Organized Convection Parameterization for the ITCZ*

BOUALEM KHOUIDER

Department of Mathematics and Statistics, University of Victoria, Victoria, British Columbia, Canada

MITCHELL W. MONCRIEFF

National Center for Atmospheric Research,+ University Corporation for Atmospheric Research, Boulder, Colorado

(Manuscript received 6 January 2015, in final form 14 April 2015)

ABSTRACT

Mesoscale convective systems (MCSs) are of fundamental importance in the dynamics of the atmospheric circulation and the climate system. They are often observed to develop over significant terrain in ambient shear flows in midlatitudes and embedded within the Madden–Julian oscillation (MJO) and convectively coupled equatorial wave (CCEW) envelopes, as well as in the intertropical convergence zone (ITCZ). Yet general circulation models (GCMs) fail to resolve these systems, and their underlying convective parameterizations are not directed to represent organized circulations. Shear-parallel MCSs, which are common in the ITCZ, have a three-dimensional structure and, as such, present a serious modeling challenge. Here, a previously developed multicloud model (MCM) is modified to parameterize MCSs. One of the main modifications is the parameterization of stratiform condensation to capture extended stratiform outflows, which characterize MCSs, resulting from strong upper-level jets. Linear analysis shows that, under the influence of a typical double African and equatorial jet shear flow, this modification results in an additional new scale-selective instability peaking at the mesoalpha scale of roughly 400 km. Nonlinear simulations conducted with the modified MCM on a 400 km × 400 km doubly periodic domain, without rotation, resulted in the spontaneous transition from a quasi-two-dimensional shear-perpendicular convective system, consistent with linear theory, to a fully three-dimensional flow structure. The simulation is characterized by shear-parallel bands of convection, moving slowly eastward, embedded in stratiform systems that expand perpendicularly and propagate westward with the upper-level jet. The mean circulation and the implications for the domain-averaged vertical transport of momentum and potential temperature are discussed.

1. Introduction

A key issue is that propagating organized convection is not represented in traditional global climate models. This process is not resolved by the order-100-km grid, and cumulus parameterization fails to take basic mesoscale circulations into account (Moncrieff 1992). The Year of Tropical Convection (YOTC) project[1] has drawn significant attention to organized convection and its parameterization (Moncrieff et al. 2012; Waliser et al. 2012). The mesoscale convective system (MCS), typically a few hundred kilometers in the horizontal scale, is a prime example of organized convection (Houze 2004; Moncrieff 2010). These systems can last for days, compared to about

* Supplemental information related to this paper is available at the Journals Online website: http://dx.doi.org/10.1175/JAS-D-15-0006.s1.

+ The National Center for Atmospheric Research is sponsored by the National Science Foundation.

[1] YOTC was jointly fostered and supported by the WCRP and WWRP-THORPEX as an international response to a 2006 workshop hosted by the International Centre for Theoretical Physics (ICTP) in Trieste, Italy, as summarized by Moncrieff et al. (2007). Originally planned for a 1-yr period when the ECMWF Integrated Forecast System (IFS) provided analysis, 10-day forecasts, and subgrid data, the period was extended for a second year (i.e., May 2008–April 2009) to capture El Niño conditions that followed the initial La Niña.

Corresponding author address: Dr. Boualem Khouider, Mathematics and Statistics, University of Victoria, P.O. Box 3045, STN CSC, Victoria BC V8W 3P4, Canada.
E-mail: khouider@math.uvic.ca

DOI: 10.1175/JAS-D-15-0006.1

an hour for cumulus convection, and propagate for thousands of kilometers, affecting the diurnal cycle of precipitation, radiative transfer, and the water cycle over land and ocean. Examples include orographic MCSs propagating in shear flow associated with midlatitude and subtropical jet streams, MCS superclusters embedded in the Madden–Julian oscillation (MJO) in particular, and convectively coupled waves in general. The NCAR and GFDL climate models show similar distributions of global precipitation bias over continents and oceans, in the monsoons over the Indian Ocean and western Pacific in association with the MJO, and in the intertropical convergence zone (ITCZ) [see Fig. 10 in Moncrieff (2010)].

Our focus on the ITCZ in this paper stems partly from the distinctive character of its convective organization. Classical MCS and squall lines are usually oriented perpendicular to the lower-tropospheric wind shear, mainly as a result of the effect of wind shear on the initiation of cumulonimbus associated by dynamic lifting at downdraft outflows (density currents), which has long been known to be important (Thorpe et al. 1982; Rotunno et al. 1988; Lafore and Moncrieff 1989).

However, shear-perpendicular systems are not the most common form of organization for the ITCZ. In the GARP Atlantic Tropical Experiment (GATE) intensive observation period conducted in the ITCZ of the eastern tropical Atlantic, shear-parallel convective bands greatly outnumbered shear-perpendicular squall lines (Houze and Cheng 1977; Cheng and Houze 1979; Dudhia et al. 1987; Dudhia and Moncrieff 1987, hereafter DM87). Nevertheless, shear-parallel bands have received remarkably little attention. Having a fundamental three-dimensional structure, shear-parallel bands are not amenable to two-dimensional simplification, in contrast to squall lines and MCSs, for which the simplest archetypal two-dimensional model (Moncrieff 1992) is widely applicable (Houze 2004). Figure 1 illustrates organized convection in conjunction with synoptic waves in the ITCZ of the eastern Pacific. Note that in this figure the convection is elongated east–west (i.e., approximately parallel to the zonal wind and the ITCZ). Classical linear small-amplitude perturbation theory (Kuo 1963) shows that the most rapidly amplifying convective instability takes the form of three-dimensional rolls aligned parallel to the shear with fastest growth at the infinitesimally short wavelength. In contrast, two-dimensional convective instability is perpendicular to the shear with maximum growth rate at finite scale. In this paper, we shall develop a novel new three-dimensional scale-selection principle for shear-parallel organized rainbands in the ITCZ that is distinct from the classical theories.

DM87 is one of the very few modeling studies that comprehensively addresses the shear-parallel organization of tropical convection. Imposed large-scale ascent (i.e., a Hadley circulation) is crucial for maintaining the quasi-stationary convective bands observed in the ITCZ region of GATE. The simulated DM87 quasi-stationary convective band, aligned approximately parallel to the low-level wind shear, occupied an environment with properties that were defined from GATE shipborne soundings. The convective organization is distinct from fast-moving squall lines aligned at right angles to the shear (Figs. 2 a,b). The simulated system bears a marked similarity to the observed bands: new cells develop on the eastern end of the band, with deeper cells to the west that travel along the band (see Fig. 2c). The vertical shear due to the strong low-level jet crucially influences the band development and orientation. A trajectory analysis in DM87 shows the three-dimensional structure of the mesoscale airflow. The transports of heat, moisture, and momentum indicate quasi balance between the large-scale ascent and cloud-induced descent on a time scale of hours. Heat sources and moisture sinks calculated using the Yanai et al. (1973) apparent-heat-source feature a bimodal vertical structure, in general agreement with observed cloud clusters.

The multicloud model (MCM) was introduced in Khouider and Majda (2006, hereafter KM06) and later refined in Khouider and Majda (2008b, hereafter KM08) as a simple model for convectively coupled waves. The MCM is based on the three cloud types that are observed to dominate the heating field of organized convective systems in the tropics: namely, congestus, deep, and stratiform cloud types (Johnson et al. 1999) evolving at meso-, synoptic, and planetary scales (Mapes et al. 2006; Kiladis et al. 2009). In the MCM, the convective heating parameterization is based on three prescribed main heating profiles: a convective heating profile with a half-sine shape that heats the whole troposphere and congestus and stratiform heating profiles with full-sine shapes that respectively heat the lower troposphere and cool the upper troposphere and cool the lower troposphere and heat the upper troposphere (Fig. 3). These three heating profiles collectively force the first and second baroclinic modes of vertical structure of the hydrostatic primitive equations with constant stratification and rigid-lid boundary conditions (KM06).

To take into account the key physical mechanisms that characterize tropical convective systems, such as the sensitivity of deep convection to tropospheric moisture and the role of convective instability, in addition to the first two baroclinic-mode shallow-water-like equations, the MCM carries an equation for vertical-averaged tropospheric moisture (anomalous vapor mixing ratio with respect to a prescribed exponential background profile) and an equation for the bulk boundary layer equivalent potential temperature. A simple piecewise linear and continuous moisture switch function is then

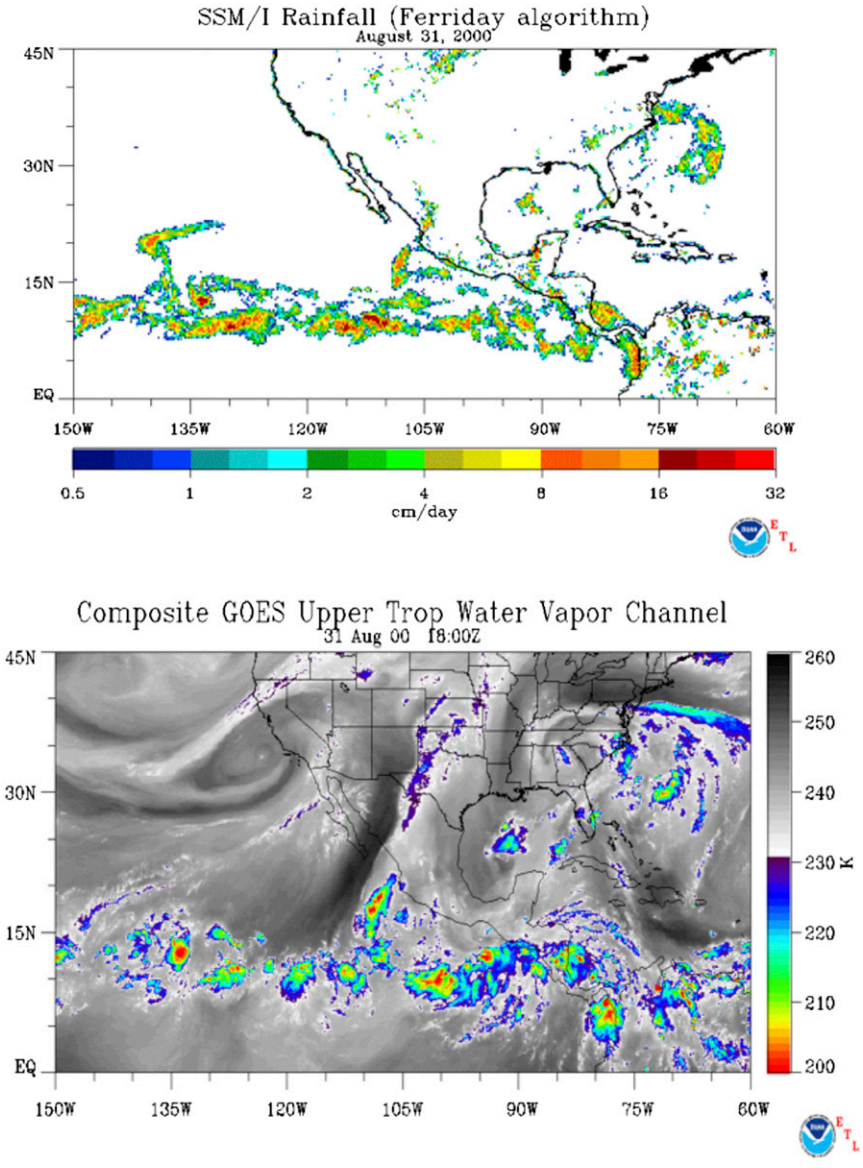

FIG. 1. Observed distribution of (top) rainfall and (bottom) precipitable water above the eastern Pacific ITCZ showing a band of mesoscale systems aligned nearly parallel to the ambient wind shear.

used to inhibit deep convection and promote congestus (low level) cloud types when the troposphere is dry and do the opposite when the troposphere moisture exceeds a certain threshold. Stratiform heating assumes an adjustment equation to deep convection with a prescribed delay time scale of 3 h, following Mapes (2000). In addition to the CAPE-based convective closure, the boundary layer thermodynamic equation is tied to the moisture equation through parameterized downdrafts that take into account the local moistening of the midtroposphere and the drying and cooling of the boundary layer mimicking cold pools. Also, during the deep convection phase, the bulk downdrafts effectively reduce CAPE, which builds up during the suppressed episode (Straub and Kiladis 2002).

In a nutshell, the mechanisms responsible for the dynamics and propagation of convectively coupled equatorial waves were built into the MCM by design, and they possess a scale-selective instability of equatorially trapped waves (Han and Khouider 2010; KM08) qualitatively matching the observed spectral peaks of tropical superclusters (Takayabu 1994; Wheeler and Kiladis 1999). Because of the observed self-similarity of convectively coupled waves, from mesoscale clusters to synoptic scales

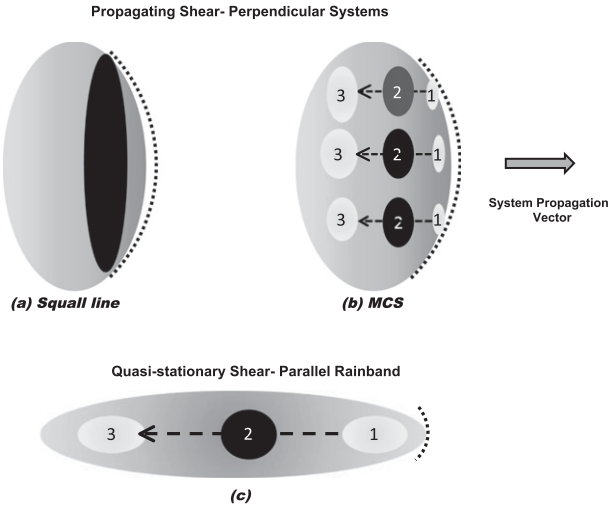

FIG. 2. Shear-perpendicular (a) squall lines and (b) mesoscale convective systems vs (c) shear-parallel systems. For the shear-perpendicular systems, the whole system is quasi steady, while the embedded convective cells move rearward with the background wind shear. The black dotted lines denote the low-level convergence of mass leading to strong localized ascent that triggers the new convection cells (denoted by 1). The cells mature into cumulonimbus (denoted by 2), and later dissipate (denoted by 3) as they travel away from the localized ascent.

to the planetary-scale intraseasonal oscillations (Mapes et al. 2006; Kiladis et al. 2009), the multicloud physics extends this spectrum of scales in both directions. In fact, without any substantial modifications, the multicloud model has been successfully used as a cumulus parameterization in an aquaplanet GCM for the simulation of convectively coupled tropical waves and intraseasonal oscillations (Khouider et al. 2011; Ajayamohan et al. 2013, 2014). Moreover, in Majda et al. (2007) and Stechmann and Majda (2009), the self-similarity feature of organized convective systems was severely tested within the MCM by effectively "pushing" the scale-selective convective instability toward planetary- and mesoscales, respectively, through a judicious choice of a few key time-scale parameter values. While the approach taken in Stechmann and Majda (2009) clearly serves its purpose, here we modify the MCM framework in order to capture simultaneously both mesoscale systems and synoptic-scale waves (i.e., within the same parameter regime).

More specifically, we build into the MCM for synoptic-scale waves new physical mechanisms that we believe are important for mesoscale system dynamics: for example, the buildup of extended stratiform cloud decks due to the return flow induced by the ambient shear in the upper troposphere. To further dissociate the stratiform anvils from the deep convection episode to allow buildup and spread of stratiform clouds, we incorporate a parameterization of stratiform condensation in the upper troposphere in addition to the stratiform adjustment component. The purpose is to enable the model to capture both leading and trailing stratiform systems (Parker and Johnson 2004);[2] the previous simple adjustment equation is suitable only for trailing stratiform clouds. One of the important modifications to the multicloud model in order to achieve this goal is the introduction of an extra layer of moisture. In addition to the boundary layer equivalent potential temperature equation, which will remain unchanged, we introduce two moisture variables corresponding to averaged moisture anomalies over the lower and upper troposphere, respectively, to replace the preexisting full-depth vertically averaged moisture.

Moreover, in order to capture the effects of a wide range of (observed) background shears, which often have complex vertical structures that are not well captured with just the first two baroclinic modes, we expand the MCM momentum and thermodynamic equations from two to four baroclinic modes. This is the minimum number of modes in order to reasonably capture the double jet (African easterly and equatorial) wind shear in DM87. Similar extension to higher baroclinic modes is also used in Stechmann and Majda (2009). We conduct a linear stability analysis and a nonlinear numerical simulation of the extended multicloud model. The linear analysis reveals that in the presence of a DM87-type shear, the new model simultaneously exhibits three scale-selective instabilities. One is at synoptic scales, inherited from the original model, which is present regardless of the presence of the shear, one is at the mesoalpha scale representing the stratiform envelope–mesoscale systems, and the third is at the mesobeta scale associated with the convection systems embedded within the stratiform outflows.

The paper is organized as follows. In section 2, we present the new multicloud model with stratiform condensation based on two moisture layers and four baroclinic-mode dynamics. The linear stability analysis, performed in two dimensions (x–z plane) along the shear direction, is presented in section 3. The results of the full three-dimensional nonlinear simulation are reported and analyzed in section 4. Section 5 concludes the paper with a few remarks and discussion.

2. The multicloud model with stratiform condensation

a. *The heating profiles and vertical mode expansion*

As pointed out in the introduction, the multicloud model is based on prescribed heating profiles for the three main

[2] Parker and Johnson (2004) divide mesoscale systems into leading, trailing, and parallel stratiform categories, depending on the location in space of the stratiform anvil clouds, with respect to the deep convection core.

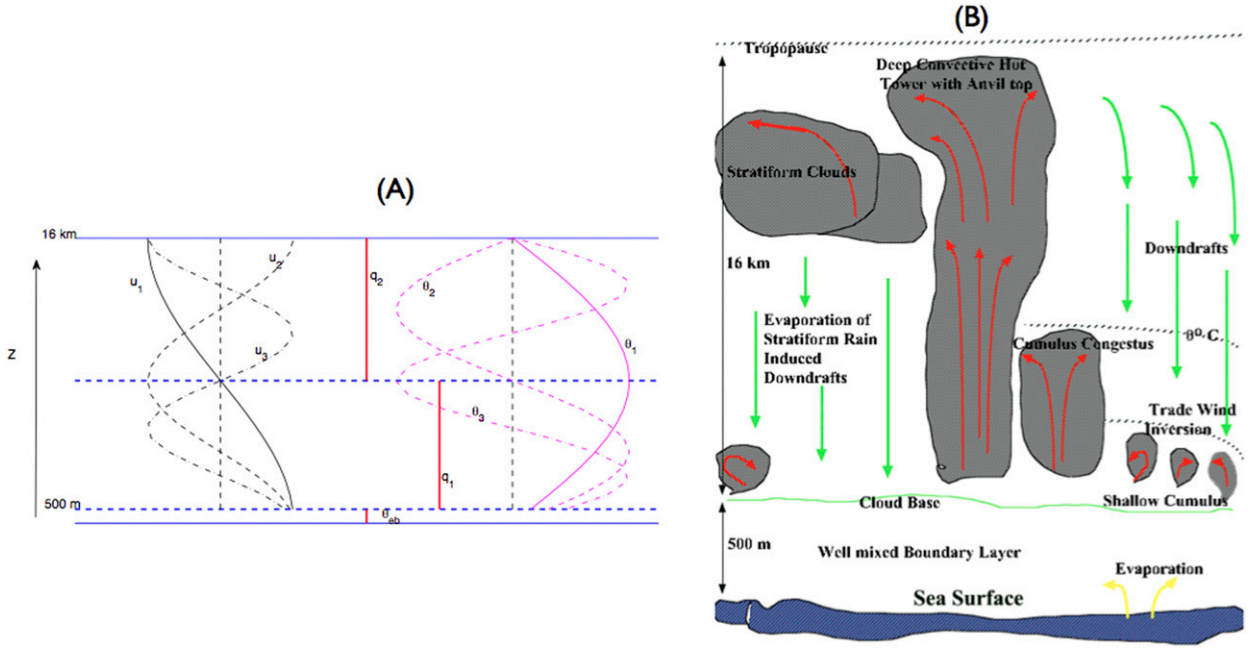

FIG. 3. (a) The first three baroclinic vertical structure functions for winds and potential temperature and the moisture anomalies. (b) A cartoon of the multicloud models illustrating the three main cloud types of diabatic heating, congestus, and stratiform, topping above the (eroded) inversion during the convective active phase. The suppressed region is dominated by shallow cumulus clouds that help drive mixing between the upper troposphere and the boundary layer moisture via the downdraft term (see text). During the active phase, the downdrafts are amplified by evaporation of stratiform rain.

cloud types—namely, congestus, deep, and stratiform—which characterize organized tropical convection (Johnson et al. 1999; KM06; KM08). In the idealized situation of a hydrostatic troposphere with constant stratification and rigid-lid boundary conditions, these take the form

$$\mathcal{H}_c = 2\sqrt{2}H_c \sin(2z), \quad \mathcal{H}_d = \sqrt{2}H_d \sin z, \quad \text{and}$$
$$\mathcal{H}_s = -2\sqrt{2}H_s \sin(2z), \tag{1}$$

so congestus and stratiform clouds heat (cool) and cool (heat) the lower (upper) and upper (lower) troposphere, respectively. Here, $\sqrt{2}$ and $2\sqrt{2}$ are normalization constants from the Galerkin projection of the primitive equations onto the baroclinic modes (Majda 2003; Khouider et al. 2013), and $0 \le z \le \pi$ is the nondimensional height coordinate, while H_c, H_d, and H_s are the parameterized heating rates (KM06; KM08).

Accordingly, we assume the following mode expansion for the fluid mechanics variables:

$$\mathbf{U} = \bar{\mathbf{u}} + \sum_{j=1}^{\infty} \sqrt{2}\mathbf{u}_j \cos(jz), \quad W = \sum_{j=1}^{\infty} \sqrt{2}w_j \sin(jz),$$
$$\text{and} \quad \Theta = \sum_{j=1}^{\infty} j\sqrt{2}\theta_j \sin(jz), \tag{2}$$

where $\mathbf{U}, \Theta$, and W are, respectively, the horizontal velocity, potential temperature, and vertical velocity, with the corresponding lowercase variables representing the associated baroclinic-mode components. For simplicity, the barotropic velocity field $\bar{\mathbf{u}}$ is set to zero here. In KM06 and KM08 and many subsequent MCM papers, the vertical expansion is truncated at $j = 2$, which is sufficient to capture the direct effect of the heating profiles. In the presence of a background shear with a more complex vertical structure, higher modes are also involved (Stechmann and Majda 2009; Khouider et al. 2012b). In particular, here, we truncate at $j = 4$. We note that by the mass continuity equation, we have $w_j = -(H/j\pi)\nabla \cdot \mathbf{u}_j$, where $j = 1, 2, \ldots$, $\nabla\cdot$ is the horizontal divergence operator, and $H = 16$ km is the fixed height of the troposphere.

The vertical structures of the multicloud dynamical and thermodynamical variables are sketched in Fig. 3, together with the assumed building block of cloud morphology, consisting of cumulus congestus, deep convective towers, and stratiform anvils that evolve above the trade wind inversion. We note that, for the sake of clarity, while only the first three baroclinic modes for winds and temperature are sketched in Fig. 3a, the present model uses four modes. The vertical profiles of deep convection, congestus, and stratiform heating are those of θ_1, θ_2, and $-\theta_2$, respectively. The moisture profile has three uniform layers,

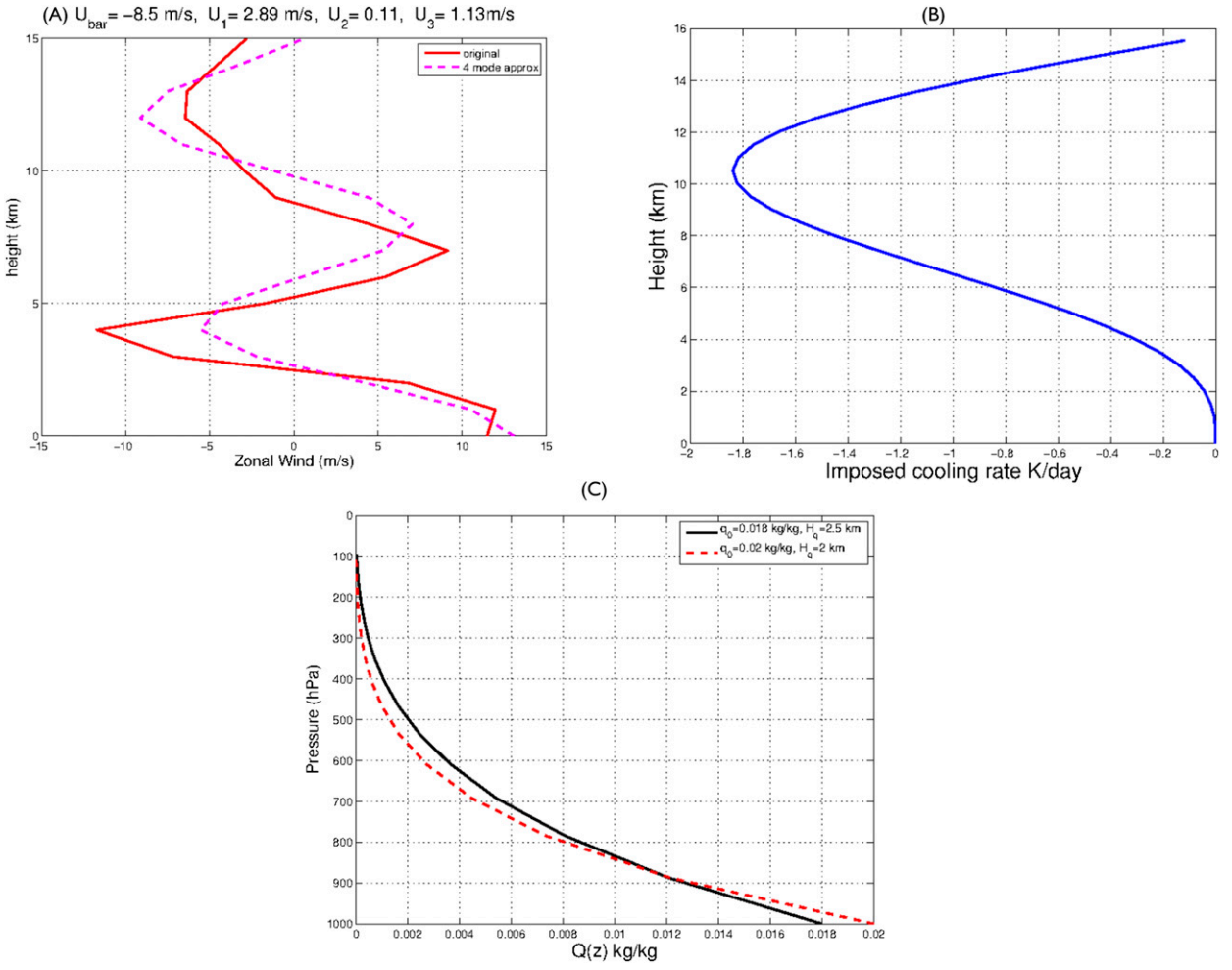

FIG. 4. (a) Background wind profile of DM87 shifted by $-8\,\mathrm{m\,s^{-1}}$ to remove the barotropic component. Original (solid) and fourth-baroclinic-mode approximation (dashed). (b) Profile of imposed cooling (see text). The moisture profiles mimic dry Sahalian- and moist non-Sahalian-air soundings. Solid lines represent $q_0 = 0.015\,\mathrm{kg\,kg^{-1}}$ and $H_d = 2.5\,\mathrm{km}$, and dashed lines represent $q_0 = 0.02\,\mathrm{kg\,kg^{-1}}$ and $H_d = 2\,\mathrm{km}$. An intermediate profile with $q_0 = 0.02\,\mathrm{kg\,kg^{-1}}$ and $H_d = 2.5\,\mathrm{km}$ is used in the present study.

represented by the equivalent potential temperature in the boundary layer θ_{eb}, the lower-tropospheric moisture q_1, and the upper-tropospheric moisture q_2, as deviations from an assumed exponential background profile (see Fig. 4c). The moisture variables are further detailed below. It should be noted that all moisture variables have been rescaled to have units of temperature (K) through multiplication by the constant L_v/C_p in order to facilitate comparison with θ_e variables.

When the hydrostatic primitive equations with constant stratification and rigid-lid boundary conditions are projected onto the first four baroclinic modes of vertical structure according to the expansions in (2) and the inner product $\langle f, g\rangle = (1/\pi)\int_0^\pi f(z)g(z)\,dz$, we obtain the following set of governing equations for the corresponding baroclinic components:

$$\frac{\partial \mathbf{u}_j}{\partial t} + \sum_{k,l=1}^{4}\left(C_{j,k,l}\mathbf{u}_k\cdot\nabla\mathbf{u}_l - S_{j,k,l}\frac{l\pi}{H}w_k\mathbf{u}_l\right) + f\mathbf{u}_j^{\perp}$$
$$= -\nabla p_j - C_d(u_0)\mathbf{u}_j - \frac{1}{\tau_R}\mathbf{u}_j \quad \text{and}$$
$$j\frac{\partial \theta_j}{\partial t} + \sum_{k,l=1}^{4}\left(lS_{k,j,l}\mathbf{u}_k\cdot\nabla\theta_l + S_{l,j,k}\frac{\pi l^2}{H}w_k\theta_l\right) + \Gamma w_j$$
$$= \delta_{1j}H_d + j\delta_{2j}(H_c - H_s) - Q_{R,j} - \frac{1}{\tau_D}\theta_j, \quad j = 1,2,3,4. \tag{3}$$

Here, the coefficients $C_{j,k,l}$ and $S_{j,k,l}$ satisfy $\sqrt{2}C_{j,k,l} = (4/\pi)\int_0^\pi \cos(kz)\cos(lz)\cos(jz)\,dz$ and $\sqrt{2}S_{j,k,l} = (4/\pi)\int_0^\pi \sin(kz)\sin(lz)\cos(jz)\,dz$ and take the values 0, ± 1, and $\delta_{kl} = 1$ if $l = k$ and 0 otherwise so that only

the first and second modes are forced by convective heating. Accordingly, we assume the radiative cooling $Q_{R,j}$ is imposed only on the first and second modes; $Q_{R,3} = Q_{R,4} = 0$. Also, $C_d(u_0)$ is the boundary layer turbulence drag coefficient with $C_d = 10^{-3}$ and $u_0 = 2\,\mathrm{m\,s^{-1}}$ while $\tau_R = 75$ days is a Rayleigh damping time scale, $Q_{R,j}$ are the baroclinic components of the prescribed uniform cooling profile, and $\tau_R = 50$ days is a Newtonian cooling time scale. Finally, $\Gamma = N^2\theta_0/g$ is the constant stratification with Brunt–Väisälä frequency $N = 0.01\,\mathrm{s^{-1}}$, $\theta_0 = 300\,\mathrm{K}$ is a reference temperature, and $g = 9.8\,\mathrm{m\,s^{-2}}$ is the gravity acceleration.

The equations in (3) are further nondimensionalized with the equatorial Rossby radius $L \approx 1500\,\mathrm{km}$ as the length scale, the first baroclinic gravity wave speed $c = HN/\pi \approx 50\,\mathrm{m\,s^{-1}}$ is the velocity scale, and $T = L/c \approx 8.33\,\mathrm{h}$ is the time scale. The temperature scale is set to $\overline{\alpha} = \Gamma H/\pi \approx 15\,\mathrm{K}$ (KM06).

b. *The two-layer moisture equations and boundary layer dynamics*

As in KM06, we decompose the moisture (vapor mixing ratio) into an exponential background moisture stratification plus a perturbation: $q = Q_0(z) + q'$ with $Q_0(z) = q_0 \exp(-z/H_q)$, where q_0 and H_q are the prescribed surface moisture and the scale height, respectively. Here, we further split the moisture perturbation into lower- and upper-tropospheric means:

$$q_1 = \frac{1}{H_m}\int_0^{H_m} q'(z)\,dz \equiv \langle q'\rangle_1 \quad \text{and}$$

$$q_2 = \frac{1}{H - H_m}\int_{H_m}^{H} q'(z)\,dz \equiv \langle q'\rangle_2 .$$

Without going into the details, when these half-tropospheric vertical averages are applied to the moisture conservation equation (KM06) under the vertical mode decomposition in (2) for the velocity field, we obtain the following equations for the lower- and upper-tropospheric moisture anomalies, separated by the midtropospheric height, which is set to $H_m = 8\,\mathrm{km}$:

$$\frac{\partial q_1}{\partial t} + \overline{\mathbf{u}}\cdot\nabla q_1 + \sum_{j=1}^{4}\tilde{\alpha}_j\nabla\cdot(q_1\mathbf{u}_j) + \sum_{j=1}^{4}\tilde{Q}_j^{(1)}\nabla\cdot\mathbf{u}_j = \frac{D}{H_m} - \frac{w_m q_m}{H_m} + \frac{(q_2 - q_1)}{\tau_{mt}} - P_1 \quad \text{and}$$

$$\frac{\partial q_2}{\partial t} + \overline{\mathbf{u}}\cdot\nabla q_2 - \sum_{j=1}^{4}\tilde{\beta}_j\nabla\cdot(q_2\mathbf{u}_j) + \sum_{j=1}^{4}\tilde{Q}_j^{(2)}\nabla\cdot\mathbf{u}_j = \frac{w_m q_m}{H - H_m} + \frac{k_m}{1 - k_m}\frac{(q_1 - q_2)}{\tau_{mt}} - P_2 . \tag{4}$$

Here, $\tilde{Q}_j^{(1)}$ and $\tilde{Q}_j^{(2)}$ are constants associated with the projection of the moisture background $Q_0(z)$ onto the four baroclinic modes over the lower and upper halves of the troposphere, while $\tilde{\alpha}_j$ and $\tilde{\beta}_j$ are associated with the perturbation q'. We have

$$\tilde{Q}_j^{(1)} = \frac{\sqrt{2}q_0}{jk_m\pi}\frac{1}{1 + j^2k_q^2\pi^2}\{jk_q\pi[1 - e^{-k_m/k_q}\cos(jk_m\pi)] - e^{-k_m/k_q}\sin(jk_m\pi)\} \quad \text{and}$$

$$\tilde{Q}_j^{(2)} = \frac{\sqrt{2}q_0}{j(1 - k_m)\pi}\frac{1}{1 + j^2k_q^2\pi^2}\{e^{-km/k_q}\sin(jk_m\pi) - jk_q\pi[(-1)^j e^{-1/k_q} - e^{-k_m/k_q}\cos(jk_m\pi)]\},$$

where $k_m = H_m/H$ and $k_q = H_q/H$, while by the mean-value-theorem approximation, $\langle q'\cos(jz)\rangle_1 \approx \tilde{\alpha}_j q_1$ and $\langle q'\cos(jz)\rangle_2 \approx \tilde{\beta}_j q_2$, $j = 1, 2, 3, 4$, we get

$$\tilde{\alpha}_j = \frac{\sqrt{2}}{jk_m\pi}\sin(jk_m\pi) \quad \text{and} \quad \tilde{\beta}_j = \frac{\sqrt{2}}{j(1 - k_m)\pi}\sin(jk_m\pi), \quad j = 1, 2, 3, 4.$$

In (4), D is the downdraft, which is assumed to balance the flux of moisture from the boundary layer through shallow convection and evaporation of stratiform rain. The terms involving $w_m q_m$ represent the exchange of moisture between the two interior layers through vertical advection, while those involving τ_{mt} account for turbulent mixing between these layers. Here, w_m and q_m are, respectively, the midtropospheric vertical velocity and moisture, given by $w_m = \sqrt{2}w_1$ and $q_m = (q_1 + q_2)/2$. The last two terms, P_1 and P_2, are the corresponding sinks of moisture due to condensational heating (i.e., precipitation).

Following KM06, the boundary layer dynamics are reduced to a single equation for θ_{eb}:

$$\frac{\partial\theta_{eb}}{\partial t} + \left(\sum_{j=1}^{4}\mathbf{u}_j\right)\cdot\nabla\theta_{eb} = \frac{1}{\tau_e}(\theta_{eb}^* - \theta_{eb}) - \frac{1}{h}D. \tag{5}$$

The last term on the right-hand side of (5) accounts for the cooling and drying of the boundary layer by the downdraft, with $h = 500\,\mathrm{m}$ the depth of the boundary layer. This is precisely the term through which cold pools and density currents can be generated in the boundary layer. The term $(1/\tau_e)(\theta_{eb}^* - \theta_{eb})$ is a bulk aerodynamic formulation of sea surface evaporation, where τ_e is an evaporation time scale and θ_{eb}^* is the saturation equivalent potential temperature in the boundary layer.

c. *The multicloud parameterization with stratiform condensation*

The modulating coefficients of the heating and cooling profiles, H_c, H_d, and H_s, in (1) are parameterized in terms of the large-scale dynamics by utilizing physical intuition. As in KM06 and KM08, the congestus heating rate is proportional to low-level CAPE (i.e., the buoyancy of an undiluted parcel integrated over the lower troposphere), while the deep convective heating is set proportional to (total) CAPE plus a Betts–Miller-like term that mimics the adjustment tendency of the moisture and temperature profiles by convection toward their reference profiles—here, a radiative convective equilibrium (RCE) solution (see below). Accordingly, we introduce the potentials for, respectively, congestus and deep convection:

$$Q_c = \left\{ \overline{Q} + \frac{\alpha_c}{\tau_c}[\theta_{eb} - a_0'(\theta_1 + \gamma_2'\theta_2 + \gamma_3'\theta_3)] \right\}^+ \quad \text{and}$$
$$Q_d = \left\{ \overline{Q} + \frac{1}{\tau_c}[a_1\theta_{eb} + a_2 q - a_0(\theta_1 + \gamma_2\theta_2 + \gamma_3\theta_3)] \right\}^+ . \tag{6}$$

Here, a_1, a_2, a_0, γ_2, γ_3, a_0', γ_2', γ_3', and α_c are nondimensional parameters and τ_c is a convective time scale (values are given in Table 3), $\overline{Q}$ is a background heating set by the RCE solution so that in (6) [and subsequently in (8)] θ_{eb}, q_1, and θ_j are deviations from RCE; and $X^+ = \max(X, 0)$. Except for the addition of θ_3, the closures in (6) are as in KM08, where a more complete discussion can be found. Moreover, as in KM06, we use a moisture switch function to inhibit deep convection when the midtroposphere is dry. With $\theta_{em} = q_1 + (2\sqrt{2}/\pi)(\theta_1 + 2\theta_2 + \theta_3)$ the vertically averaged equivalent potential temperature over the lower half of the troposphere,[3] we set $\Lambda = 1$ if $\theta_{eb} - \theta_{em} > \theta^p$ and $\Lambda = 0$ if $\theta_{eb} - \theta_{em} < \theta^m$; Λ is a piecewise linear and continuous function of $\theta_{eb} - \theta_{em}$. The threshold values θ^p and θ^m are given in Table 1. The congestus and deep convective heating rates are thus given by

$$H_c = \Lambda Q_c \quad \text{and} \quad H_d = (1 - \Lambda)Q_d . \tag{7}$$

As aforementioned, the novelty here, in terms of convective parameterization, is the introduction of a stratiform condensation parameterization. We assume that the stratiform heating is comprised of a stratiform adjustment term $H_{s,1}$ and a large-scale condensation term $H_{s,2}$. Following Mapes (2000), the stratiform adjustment term is directly tied to deep convection heating and is considered here to be unresolved stratiform anvils that lag deep convection. On the other hand, $H_{s,2}$ represents the large-scale/stratiform condensation of water vapor in the upper troposphere. It is how the model responds to upper-level moisture q_2 variability. Specifically, we set

$$H_s = sH_{s,1} + (1 - s)H_{s,2}, \quad \frac{\partial H_{s,1}}{\partial t} = \frac{1}{\tau_{sa}}(\alpha_s H_d - H_{s,1}),$$
$$\text{and} \quad H_{s,2} = \frac{1}{\tau_{sc}}\left[q_2 - \hat{q}_0 - \gamma_s \sum_{j=1}^{3} \beta_j \theta_j \right]. \tag{8}$$

Here, α_s, τ_{sa}, and τ_{sc} are respectively the stratiform adjustment parameter, adjustment time scale, and condensation time scale (values used here are given in Tables 1 and 3). The coefficients $\gamma_s = 1$ and $\beta_j = j\sqrt{2}\sin(3j\pi/4)$ so that the associated summation is a good approximation for the saturation equivalent potential temperature in the upper troposphere. In the first equation, $0 \le s \le 1$, which sets the relative strengths of $H_{s,1}$ and $H_{s,2}$. In the original MCM (e.g., KM06; KM08) $s = 1$, which sets the contribution of $H_{s,2}$ to zero. When $s = 0$, only condensation stratiform is active, but we will use a conservative value of $s = 0.25$ to allow some adjustment stratiform as well. This is in contrast with conventional GCMs, where the parameter s is effectively zero, since stratiform rain is assumed to come only from large-scale condensation.

Finally, with $k_m = 1/2$, the downdraft flux and the precipitation rates in moisture equations (4) and (5) are given respectively by (KM06; KM08)

$$D = \frac{m_0}{\overline{Q}}[\overline{Q} + \mu(H_s - H_c)]^+(\theta_{eb} - \theta_{em}) \quad \text{and}$$
$$P_1 = \frac{2\sqrt{2}}{\pi}[H_d - 2(H_s - H_c)], P_2 = \frac{2\sqrt{2}}{\pi}[H_d + 2(H_s - H_c)]. \tag{9}$$

It should be noted that P_1 and P_2 are simply the vertically averaged total heating [see (1)] over the lower and upper troposphere, respectively.

The set (2)–(9) defines the new multicloud model with 2.5 moisture levels and condensation stratiform for parallel mesoscale systems in the presence of a background vertical shear mimicking both the African and equatorial easterly jets used in DM87.

d. *Radiative convective equilibrium and the background shear*

An RCE is defined as a time and space homogeneous solution that solves the MCM equations (KM06; KM08). Denoting the RCE value of the variable X as $\overline{X}$ here, an RCE solution is defined by

[3] KM06 and KM08 use the full-tropospheric vertical average.

TABLE 1. List of physical parameters and corresponding RCE values for reference case.

Parameters		RCE values	
$H = 15.75$ km	Tropospheric height	$\overline{\Lambda} = 0.1$	Low-level troposphere index of dryness
$h = 500$ m	Boundary layer depth	$\tau_e = 8.46$ h	Evaporative time scale
$C_d = 0.001$	Turbulence drag coefficient	$\overline{Q} = 1.1111$ K day^{-1}	Available deep and congestus heating potential
$u_0 = 2$ m s^{-1}	Strength of turbulent fluctuations in boundary layer	$\overline{H}_d = 1$ K day^{-1}	Deep convection
$N = 0.01$ s^{-1}	Väisälä buoyancy frequency	$\overline{D}/H_m = 1.8006$ K day^{-1}	Downdraft moistening in lower troposphere
$\theta_0 = 300$ K	Reference temperature	$m_0 = 0.014$ m s^{-1}	Downdraft flux velocity scale
$g = 9.8$ m s^{-2}	Gravity acceleration	$\tau_{mt} = 3.5543$ h	Midtropospheric moisture mixing time scale
$\theta^p = 20$ K, $\theta^m = 10$ K	Thresholds for moistening and drying of middle troposphere	$\overline{D}/h = 1.1817$ K h^{-1}	Boundary layer downdraft cooling and drying
$H_m = H/2$	Height of lower-level tropospheric moisture layer		
$Q_{R,1} = 1$ K day^{-1}	Prescribed radiative cooling associated with first baroclinic	$\overline{H}_c = 0.1111$ K day^{-1}	Congestus heating
$Q_{R,2} = -0.25$ K day^{-1}	Prescribed radiative cooling associated with second baroclinic	$\overline{H}_s = 0.3611$ K day^{-1}	Total stratiform heating
$\theta^*_{eb} - \overline{\theta}_{eb} = 10$ K	Discrepancy between boundary layer θ_e and its saturation value at RCE		
$\overline{\theta}_{eb} - \theta_{em} = 11$ K	Discrepancy between boundary layer and midlevel tropospheric θ_e values at RCE	$H_{s,2} = 0.25$ K day^{-1}	Adjustment stratiform heating
$L_w = 2260$ kJ kg^{-1}	Latent heat of vaporization	$\tilde{Q}^{(1)}_{1,2,3} = 1.9129, 1.3662, 0.8301$	Coefficients of $\nabla \cdot \mathbf{u}_{1,2,3}$ in q_1 equation.
$C_p = 1.012$ kJ kg^{-1} K^{-1}	Heat capacity at constant pressure of dry air	$\tilde{Q}^{(2)}_{1,2,3} = 0.1760, -0.0585, -0.0246$	Coefficients of $\nabla \cdot \mathbf{u}_{1,2,3}$ in q_2 equation.
$q_0 = 0.02 L_w/C_p$ K	Boundary layer reference moisture		
$H_q = 2.5$ km	Moisture background scale height		
$\alpha_s = 0.25$ km	Adjustment ratio of stratiform heating		
$\overline{q}_1 - \overline{q}_2 = 0.2$ K	Discrepancy between low-level and top-level moisture content		

$$\overline{H}_d = Q_{R,1}, \overline{H}_c - \overline{H}_s = Q_{R,2}, \frac{1}{\tau_e}(\theta^*_{eb} - \overline{\theta}_{eb}) = \frac{1}{h}\overline{D}, \frac{1}{H_m}\overline{D} + \frac{1}{\tau_{mt}}(\overline{q}_1 - \overline{q}_2) = \frac{2\sqrt{2}}{\pi}[\overline{H}_d - 2(\overline{H}_s - \overline{H}_c)],$$

$$\overline{H}_{s,1} = \alpha_s \overline{H}_d, \quad \text{and} \quad \frac{1}{\tau_{mt}}(\overline{q}_1 - \overline{q}_2) = \frac{2\sqrt{2}}{\pi}[\overline{H}_d + 2(\overline{H}_s - \overline{H}_c)]. \tag{10}$$

Thus, given the radiative forcing components, $Q_{R,1}$ and $Q_{R,2}$; the mean deviation of the equivalent potential temperature in the boundary layer and its saturation value, $\theta^*_{eb} - \overline{\theta}_{eb}$; the mean deviation between the boundary layer and midtropospheric θ_e, $\overline{\theta}_{eb} - \overline{\theta}_{em}$; and the mean deviation between the upper- and lower-troposphere moisture, $\overline{q}_1 - \overline{q}_2$, the RCE solution constrains a few key parameters for the MCM. Namely, we have

$$\tau_e^{-1} = \frac{2\sqrt{2}}{\pi}\frac{H}{h}\frac{Q_{R,1}}{\theta^*_{eb} - \overline{\theta}_{eb}}, \quad \overline{Q} = \frac{1}{1-\overline{\Lambda}}Q_{R,1},$$

$$m_0 = \frac{2\sqrt{2}HQ_{R,1}}{(1 + Q_{R,2}/\overline{Q})(\overline{\theta}_{em} - \overline{\theta}_{eb})}, \quad \text{and}$$

$$\tau_{mt} = \frac{\pi(\overline{q}_1 - \overline{q}_2)}{2\sqrt{2}(Q_{R,1} + 2Q_{R,2})}.$$

The RCE is an integrated part of the background, the external parameters of which are typical for the tropics (KM06; KM08). The RCE, the constant stratification, the moisture background $Q(z)$, and the background shear form the main environment where convectively coupled waves of distinct scales can grow and propagate. As pointed out above, our model of a background shear mimics the double jet used by DM87. The solid line in Fig. 4a approximates DM87's original shear flow, while the dashed line represents its projection onto the first four baroclinic modes of vertical structure in (2). Four modes are the minimum that could reasonably capture the double jet. Figure 4b shows the imposed total radiative cooling $[Q_R(z) = \sqrt{2}Q_{R,1}\sin(z) + 2\sqrt{2}Q_{R,2}\sin(2z)]$ for the values of $Q_{R,1}$ and $Q_{R,2}$ given in Table 1, and Fig. 4c shows two background moisture profiles corresponding to two sets of parameters q_0 and H_d in (3). The intermediate set of values $q_0 = 0.02\,\mathrm{kg\,kg^{-1}}$ and $H_q = 2.5\,\mathrm{km}$ (profile not shown) is used in this study, mimicking the mixture of dry Sahalian and moist non-Sahalian soundings reported in Dunion and Marron (2008) from the North Atlantic and Caribbean Sea regions; the two profiles shown in Fig. 4 mimic roughly the two extremes.

3. Two-dimensional linear theory

In this section, we address wavelike disturbances that are small perturbations of the mean RCE solution and the mean wind and moisture profiles in Fig. 4. We thus consider the linearized 2D (x, z) equations with respect to this background. We have

$$
\begin{aligned}
&\frac{\partial u_j}{\partial t} - \frac{\partial \theta_j}{\partial x} + \sum_{l=1}^{3}\left(\sum_{k=1}^{4} A^{u}_{jkl}U_k\right)\frac{\partial u_l}{\partial x} + B_{jj}u_j = 0, \quad j = 1,2,3,\\
&\frac{\partial \theta_j}{\partial t} - \frac{1}{j^2}\frac{\partial u_j}{\partial x} + \sum_{l=1}^{3}\left(\sum_{k=1}^{4} A^{\theta}_{jkl}U_k\right)\frac{\partial \theta_l}{\partial x} = C'_j - \frac{1}{\tau_D}\theta_j, \quad j = 1,2,3,\\
&\frac{\partial q_j}{\partial t} + \left(\sum_{k=1}^{4} A^{q}_{jkl}U_k\right)\frac{\partial q_j}{\partial x} + \sum_{l=1}^{2} B^{q}_{j0l}q_l + \sum_{j=1}^{3}\tilde{Q}^{(i)}_j\frac{\partial u_j}{\partial x} = (2-j)\frac{D'}{H_m} - P'_j, \quad j = 1,2,\\
&\frac{\partial \theta_{eb}}{\partial t} + \sqrt{2}\left(\sum_{j=1}^{4} U_j\right)\frac{\partial \theta_{eb}}{\partial x} = -\frac{1}{\tau_e}\theta_{eb} - \frac{1}{h}D', \quad \text{and} \quad \frac{\partial H_{s,1}}{\partial t} = \frac{1}{\tau_{sa}}(\alpha_s H'_d - H_{s,1}).
\end{aligned}
\tag{11}
$$

Here, $C'_1 = H'_d, C_2 = H'_c - H_s$, and $C'_3 = 0$ with the primed variables representing linear deviations of the various forcing terms from their background state values. They are listed in Table 2 for completeness.

We seek solutions for the linear equations in (11) of the form $\mathbf{W} = \hat{\mathbf{W}}e^{kx-\omega t}$, where $\mathbf{W}$ represents the 10-dimensional vector field of prognostic variables, $\mathbf{W} = (u_j, \theta_j, q_1, q_2, \theta_{eb}, H_{s,1})$, $j = 1, 2, 3$. Here, $\hat{\mathbf{W}}$ is a constant vector, while k and ω are, respectively, the wavenumber and frequency. When this ansatz is plugged into (11), we obtain an eigenvalue problem of the form $\omega\hat{\mathbf{W}} = (k\mathbf{A} + i\mathbf{B})\hat{\mathbf{W}}$, where $\mathbf{A}$ and $\mathbf{B}$ are constant matrices whose entrees depend on the model parameters listed in Tables 1 and 3 and elsewhere in the text, including the background shear profile components U_1, U_2, U_3, and U_4. We note that only three baroclinic modes are used for the perturbations u_j and θ'_j in (11). This is because without the nonlinear transport terms, the fourth mode does not feed back onto the rest of the model; it becomes a slaved mode, and thus it is ignored in the linear analysis.

As a consistency test, we first consider the case of zero background shear, $U_1 = U_2 = U_3 = U_4 = 0$, to ensure that, despite the considerable changes of including a second moisture layer and a stratiform condensation term, the MCM still captures the scale-selective synoptic-scale instabilities of convectively coupled gravity waves (KM06; KM08). As illustrated in Figs. 5a and 5b, under the standard parameters in Tables 1 and 3 (which are in the bulk of those used in KM08, except for the new parameters specific to this extended model), the new model exhibits the same instability band as in KM08, corresponding to synoptic-scale convectively coupled gravity waves ($\beta = 0$ here) traveling in both directions at roughly $17\,\mathrm{m\,s^{-1}}$. However, the instability extends to small scales with constant growth rates and significantly reduced phase speed that vanish when $k \to \infty$. The new model does not significantly alter the dynamics and physical features of the MCM. However, as demonstrated below, the new model exhibits a new instability for mesoscale convective systems in addition to the synoptic-scale waves when the background shear is activated.

The small and steadily growing modes at small scale are easily stabilized by adding a hyperviscosity term of the form $-\nu|\nabla|^4\mathbf{W}$ to the prognostic equations. From

TABLE 2. Linearized forcing terms.

$$H'_d = (1-\overline{\Lambda})\frac{1}{\tau_c}(a_1\theta_{eb}a_2 + q_2 - a_0\theta_1 - a_0\gamma_2\theta_2 - a_0\gamma_3\theta_3) - \overline{Q}A_\Lambda\left[\theta_{eb} - q_1 - \frac{2\sqrt{2}}{\pi}(\theta_1 + \alpha_2\theta_2 + \alpha_3\theta_3)\right]$$

$$H'_c = \overline{\Lambda}\frac{\alpha_c}{\tau_c}(\theta_{eb} - a'_0\theta_1 - a'_0\gamma'_2\theta_2 - a'_0\gamma_3\theta_3) + \overline{Q}A_\Lambda\left[\theta_{eb} - q_1 - \frac{2\sqrt{2}}{\pi}(\theta_1 + \alpha_2\theta_2 + \alpha_3\theta_3)\right]$$

$$H'_{s,1} = \frac{1}{\tau_{sc}}\left(q_2 - \gamma_s\sum_{j=1}^{3}\beta_j\theta_j\right)$$

$$D' = m_0\left(1 - \mu\frac{Q_{R,2}}{\overline{Q}}\right)\left[\theta_{eb} - q_1 - \frac{2\sqrt{2}}{2}\pi(\theta_1 + \alpha_2\theta_2 + \alpha_3\theta_3)\right] + \frac{m_0(\overline{\theta}_{eb} - \overline{\theta}_{em})}{\overline{Q}}\mu[sH'_{s,1} + (1-s)H_{s,2} - H'_c]$$

$$P'_1 = \frac{\sqrt{2}}{k_m\pi}[c_{1m}H'_d - c_{2m}(H'_s - H'_c)]$$

$$P'_2 = \frac{\sqrt{2}}{(1-k_m)\pi}[\overline{c}_{1m}H'_d + c_{2m}(H'_s - H'_c)]$$

$$\overline{\Lambda} = A_\Lambda(\overline{\theta}_{eb} - \overline{\theta}_{em}) + B_\Lambda$$

$A_\Lambda = 1/(\theta^+ - \theta^-)$ and $B_\Lambda = -\theta^-/(\theta^+ - \theta^-)$ if $\theta^- < \overline{\theta}_{eb} - \overline{\theta}_{em} < \theta^+$,
$\overline{\Lambda} = 1$ and $A_\Lambda = 0$ if $\overline{\theta}_{eb} - \overline{\theta}_{em} > \theta^+$ and $\overline{\Lambda} = 0$ and $A_\Lambda = 0$ if $\overline{\theta}_{eb} - \overline{\theta}_{em} < \theta^+$.

now on, such a viscosity term with the viscosity coefficient $\nu = 10^{-3}\,\mathrm{m^{-4}\,s^{-1}}$ is systematically applied.

In Figs. 5c and 5d, we show the phase [Re(ω)] and growth rates [Im(ω)] for the background wind shear in (2), which is adapted from DM87. The rest of the parameters are as in Figs. 5a and 5b. As we can see, the background shear results in two significant changes. First, in addition to the robust synoptic-scale instability band peaking roughly at wavenumber 20 and the persistence of the small-scale and (previously) nearly standing branch, a new scale-selective instability branch occurs at the mesoalpha scale ($k \approx 120$). Second, there is a symmetry breaking in the sense that the eastward-moving synoptic-scale waves are more unstable than their westward counterparts, and all eastward waves are unstable for wavenumbers of roughly 30 or larger. (Note that the large wavenumbers are effectively stabilized through the addition of the small hyperviscosity term without affecting the larger-scale dynamics.) The smaller-scale instability branch remains, but it is now associated with nonzero-phase-speed waves moving at roughly $17\,\mathrm{m\,s^{-1}}$. It is also interesting to note that because of imposed Doppler shift, the eastward synoptic-scale waves now move at about $25\,\mathrm{m\,s^{-1}}$ (at their instability peak), while the westward ones move much slower, at about $-10\,\mathrm{m\,s^{-1}}$ (i.e., instability at the mesobeta scale). In physical terms, the mesoalpha instability corresponds to the shear-driven mesoscale systems, (i.e., the parallel lines reported in DM87), while the mesobeta-scale instability is associated with the individual convective storms that form inside the mesoscale system. This is confirmed by the nonlinear simulation in section 4.

While the synoptic-scale waves are essentially identical to those in the original multicloud model (KM06; KM08), the instabilities at smaller scales are novel and deserve close attention. An important question, however, remains: whether and how the latter instabilities are related to the mesoscale instabilities reported in Stechmann and Majda (2009) and Khouider et al. (2012b). Nonetheless, the key novelty here is the coexistence of these two instabilities at the same time and on different branches. We note that, while the two waves move eastward in the direction of the low-level wind, near its instability peak, the mesoalpha wave is nearly standing with respect to a steering level near the surface, while the mesobeta waves move at a faster speed of about $17\,\mathrm{m\,s^{-1}}$. Noting that a barotropic (vertically uniform) component of roughly $-10\,\mathrm{m\,s^{-1}}$ has been removed from the original DM87 wind profile (see Fig. 4a), the mesoalpha waves mimic the mesoscale system envelope simulated in DM87, while the mesobeta instability represents the convective elements that evolve and propagate within the envelope. This is corroborated in section 4.

The tunable model parameters are listed in Table 3. Space limitation precludes a thorough sensitivity analysis of all these parameters here, but many are inherited from the original MCM and are extensively studied in the subsequent publications (KM08; Majda et al. 2007; etc.). Although, their effect on the presently modified model can be quantitatively different, the physical mechanisms that they represent and their effect on the model behavior remain qualitatively the same. Here, we summarize the effect of changing some key parameters that are more pertaining to the new upper-level moisture and the associated stratiform condensation parameters. More specifically, we vary the

TABLE 3. List of tunable parameters and their standard values.

Parameter	Description
$s = 0.25$	Contribution of deep convection adjustment to stratiform heating
$1 - s = 0.75$	Contribution of large-scale condensation to stratiform heating
$\tau_{sa} = 3$ h	Stratiform heating adjustment time scale
$\tau_{\text{conv}} = 2$ h	Convective time scale
$\alpha_c = 0.25$	Ratio of deep convective and congestus time scales
$\tau_{sc} = 3$ h	Stratiform condensational heating time scale
$\tau_D = 50$ days	Newtonian cooling relaxation time scale
$\tau_R = 75$ days	Rayleigh wind relaxation scale
$a_1 = 1$	Coefficient of θ_{eb} in deep convection closure
$a_2 = 1 - a_1$	Coefficient of q_1 in deep convection closure
$a_0 = 5$	Coefficient of θ_1 in deep convection closure
$a_0' = 2$	Coefficient of θ_1 in congestus closure
$\gamma_2 = 0.25$	Relative contribution of θ_2 to Q_d
$\gamma_3 = 1.0$	Relative contribution of θ_3 to Q_d
$\gamma_2' = 2.0$	Relative contribution of θ_2 to Q_c
$\gamma_3' = 1$	Relative contribution of θ_3 to Q_c
$\gamma_s = 1$	Coefficient of θ_1 of convective stratiform closure
$\beta_1 = 1$	Relative contribution of θ_1 to stratiform convection
$\beta_2 = -2\sqrt{2}$	Relative contribution of θ_2 to stratiform convection
$\beta_3 = 3$	Relative contribution of θ_3 to stratiform convection
$\mu = 0.25$	Relative contribution of $H_s - H_c$ to downdrafts

parameters H_q, s, and $\overline{q}_1 - \overline{q}_2$. We note that the latter is not listed in Table 3 as a tunable parameter, being an imposed RCE variable, but we found the model sensitive to its value. Table 4 shows the maximum growth rates and associated wavenumbers for both the mesoalpha and the synoptic unstable modes for shifts from the standard values $H_q = 0.5$ km, $s = 0.25$, and $\overline{q}_1 - \overline{q}_2 = 0.1$ K.

We note that increasing H_q causes the growth rate of the mesoalpha mode to decrease and that of the synoptic mode to increase by a comparable amount, while increasing $\overline{q}_1 - \overline{q}_2$ has the opposite effect. Also, for both parameters, the maximum-growth wavenumber seems to move toward larger scales with increasing instability for the mesoalpha mode and toward smaller scales as the growth rate decreases. These two parameters seemingly have the same sensitivity relations, consistent in that both relate to the vertical gradient of moisture in the middle troposphere. The larger gradient displays a stronger instability for the mesoalpha mode, a weaker instability for the synoptic mode, while smaller moisture gradients lead to a weaker mesoscale instability and stronger synoptic instability. On the other hand, the parameter s implies a stronger mesoalpha mode for larger values of $1 - s$ and smaller values of s, as well as the same tendency as in the previous two cases for the maximum growth wavenumber. That the instability of the mesoalpha mode increases with the increasing values of $1 - s$ confirms our intuition that the stratiform condensation heating is particularly important.

4. Nonlinear simulation: Transition from shear-perpendicular to shear-parallel lines

Here we conduct numerical simulations using the extended multicloud model with four baroclinic modes, two moisture layers in the free troposphere, and stratiform condensation presented in section 2: namely, (3)–(9) supplemented by Tables 1 and 3. We note that, unlike the multicloud nonlinear simulations presented in Khouider and Majda (2007) and KM08, here the nonlinear advection terms are retained. We use a square domain of 400 km × 400 km with periodic boundary conditions and no rotation ($f = 0$). We use a fourth-order finite-difference essentially nonoscillatory scheme (Kacimi and Khouider 2013) in space and an explicit fourth-order Runge–Kutta method in time. The discretization grid consists of 100 × 100 points in space and a time step $\Delta t = 1$ min.

As initial conditions, we use the background RCE solution, including the background wind shear (for the zonal velocity) plus a (strong) perturbation consisting of the linear solution corresponding to the mesoalpha instability at wavenumber $k = 100$ so its wavelength matches the computational domain. Since the linear solution is independent of y, the initial condition is set to be uniform in y: $\mathbf{W}(x, y, 0) = \overline{\mathbf{W}} + \epsilon \text{Re}[\hat{\mathbf{W}} e^{ikx}]$. We note that the same linear solution was used to validate the code. Here, x is the coordinate in the background wind direction (east–west), and y (north–south) is perpendicular to x.

In Fig. 6, we plot the root-mean-square (RMS) of all the prognostic variables as a function of time after a simulation period of 20 days. Unless otherwise specified, all the parameters are as reported in Tables 1 and 3. From Fig. 6, we can see that, after a transient period of about 7 days, the solution enters a quasi-steady oscillatory regime, suggesting a new statistical equilibrium characterized by strong wave activity. In Fig. 7, we plot the Hovmöller diagrams of the congestus, deep, and two stratiform heating rates averaged in the y direction, which is the direction parallel to the background wind shear.

Comparing Figs. 6 and 7, we can see that the transient period of roughly 150 h is associated with a more or less linear regime where we see essentially a slowly propagating envelope of convection in which fast-moving streaks evolve and a clearly delimited suppressed phase outside the envelope. This is, in fact, the persistence of the initial linear solution, which now acts as an envelope for small-scale convective events associated with the mesobeta instability. This feature is more

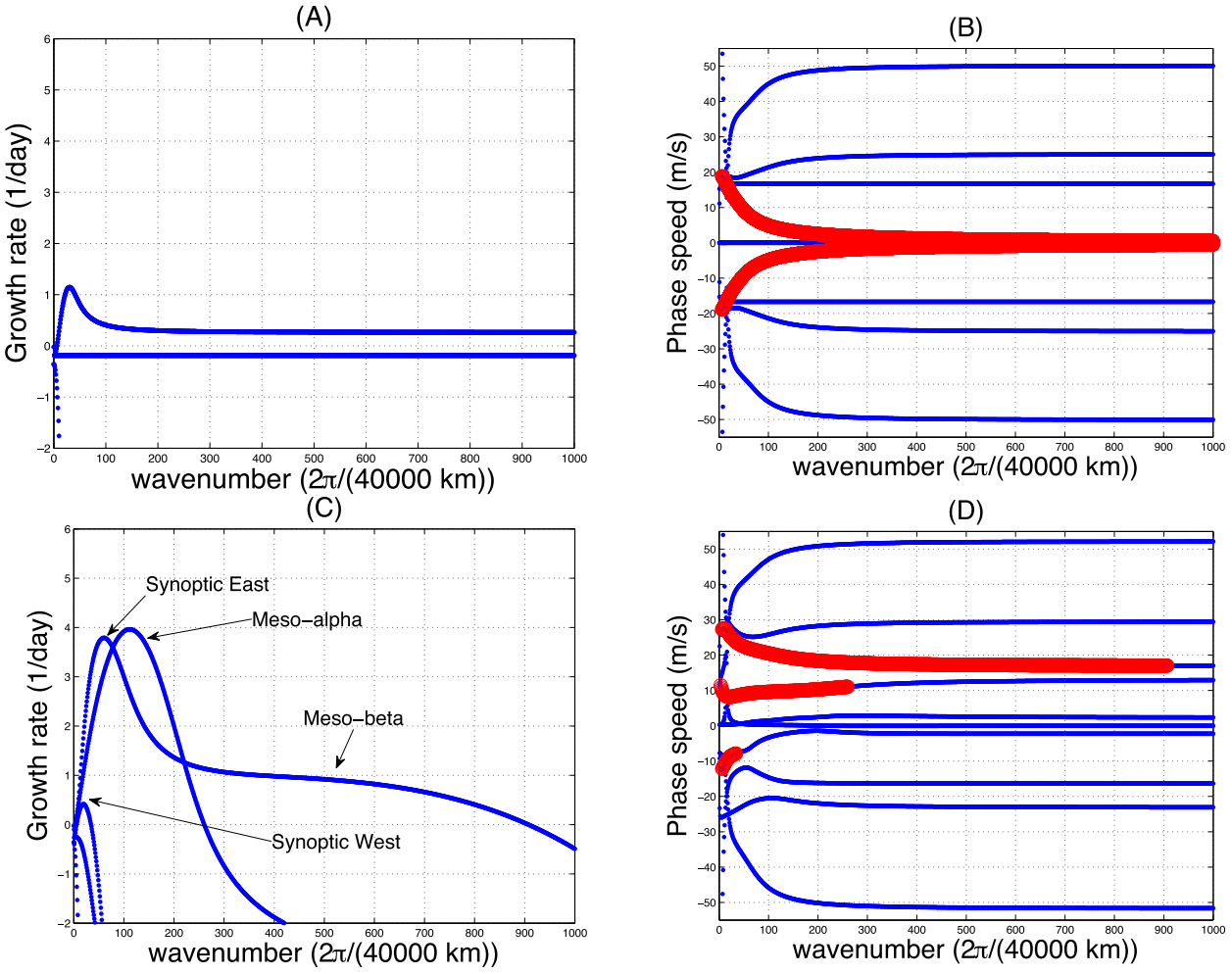

FIG. 5. (a),(c) Growth rates and (b),(d) phase speed as functions of the wavenumber for (a),(b) the case without a background shear and (c),(d) the DM87 background shear. The red circles in (b) and (d) identify modes with positive growth rates. In (c) and (d), a hyperviscosity term is added to the system to stabilize the small scales (see text for details).

visible in Figs. 7a–c; the parameterized large-scale stratiform condensation seems to be dissociated, as it appears to invade, at times, the region of suppressed convection. Consistently, after this transition period, the solution enters a new regime where convection and large-scale stratiform condensation play completely different roles. Before detailing this new phenomenon, we can readily see from Fig. 7 that, while the congestus, deep, and adjustment stratiform heating rates consistently exhibit eastward-moving streaks with a phase speed of roughly $4\,\mathrm{m\,s^{-1}}$, the large-scale stratiform condensation shows streaks moving in the opposite direction at higher speed of $-12\,\mathrm{m\,s^{-1}}$.

To gain more insight into the dynamics that take place before and after the transition, we plot in Fig. 8 a few snapshots of the horizontal distribution (x, y; x being the direction parallel to the shear) of H_c, H_d, and $H_{s,2}$ at five successive times: 50, 280, 290, 300, and 479 h. The first instance (Figs. 8a,f,k) is within the transient period. It illustrates a clear shear-perpendicular line (see Fig. 2), which moves eastward according to Fig. 7, with congestus leading deep convection, while stratiform (large-scale condensation) is lagging behind. This is reminiscent of perpendicular line systems with lagging stratiform anvils, according to Parker and Johnson's (2004) terminology.

From Fig. 7, we can see that, during this transient period, the system consists of a slowly moving envelope and embedded faster-moving smaller-scale convective peaks associated respectively with the mesoalpha and mesobeta instabilities reported in Fig. 5. However, the fact that this system is aligned perpendicular to the shear is inherited from the initial conditions. The following three instances (Figs. 8b–d, 8g–i, and 8l–n) correspond

TABLE 4. Sensitivity to key parameters for the 2D linear model.

None	Standard	3.96	112	3.79	60
H_q	2 km	4.60	103	3.43	59
H_q	3 km	3.46	115	4.08	62
$\overline{q}_1 - \overline{q}_2$	0.1 kg kg^{-1}	2.60	123	4.33	71
$\overline{q}_1 - \overline{q}_2$	0.3 kg kg^{-1}	4.77	102	3.26	54
s	$s = 1 - s = 0.5$	1.75	78	3.25	55
s	$s = 0$, $1 - s = 1$	5.67	134	4.15	64

to three successive snapshots within the statistical quasi-steady-state regime. They display elongated streaks of deep convection parallel to the shear direction. Although thorough insight was gained from animations (see supplemental material), the snapshots illustrate the main structural feature. While the deep convection streaks move to the right and evolve within a narrow channel located roughly between $y = 0$ and 50 km, the corresponding congestus and stratiform heating peaks evolve on the northern and southern flanks of this channel, with the stratiform contours occasionally expanding outside the channel in the perpendicular direction. Also, as can be surmised from these pictures, the congestus signals appear to move eastward (to the right) and somewhat lead the convective streaks (recall the periodic boundary conditions); the extended stratiform regions move to the left (i.e., in the opposite direction). This is a good example of shear-parallel mesoscale lines of convection evolving in a mesoscale stratiform system, as depicted in Fig. 4. The last instance is at the end of the simulation to showcase the perpetuation of the picture just illustrated.

To help elucidate the cause and effect of the heating dynamical distribution, we show in Fig. 9a the contour of zonally averaged mean zonal wind averaged between times $t = 7$ and 20 days. As we can see, while the mean conserves somewhat its initial shape over most of the y domain, it is severely altered within the narrow region between $y = 0$ and 50 km, corresponding roughly to the channel where the deep convection streaks evolve in Fig. 8. A few slices of this mean zonal wind are plotted in Fig. 9b (solid lines), corresponding roughly to two locations outside and far from the channel ($y = -148$ and 156 km) and one near the center of the (virtual) channel (at $y = 28$ km). Figure 9b (bottom right) shows the average over the y domain (i.e., the horizontally averaged mean wind). The dashed line in each subpanel represents the original/initial DM87 background wind in Fig. 4. The full-domain average shows a markedly significant deviation from the initial background wind profile especially visible in the severe reduction of the lower-level jet. This and the strong disruption of the background in the region of deep convection (Fig. 9b) constitute a significant upscale effect of convective momentum transport (CMT), which clearly cannot be captured by general circulation models and is not usually taken into account by the underlying cumulus parameterization.

Also it is worthwhile noting that the westward (to the left) propagation of the extended stratiform heating is mainly due to the advection of q_2 by the upper-tropospheric jet, which points in that direction. Not only is this jet weaker in the region of deep convection, but deep and congestus heating is essentially driven by the lower-tropospheric moisture and the boundary layer potential temperature, which are both advected eastward by the near-surface wind. This, in essence, explains why in Fig. 7 the deep and congestus streaks move eastward while the large-scale condensation stratiform anvils ($H_{s,2}$) move westward.

In Figs. 9c and 9d, we represent the mean wind pattern in the y–z directions on top of the contours of the total heating [see (1); $Q = \mathcal{H}_d + \mathcal{H}_c + \mathcal{H}_s$] and the vertical velocity [see (2)]. As we can see, the deep convection activity that takes place along the channel in the background wind sets up a local Hadley circulation with a meridional wind maximum comparable to observed values, of a few meters per second. Another important aspect of Figs. 9c and 9d resides in the similarities and differences in the patterns of the heating and vertical velocity. First, the region of deep convective heating coincides with the rising branch of the local Hadley cell. Second, there are two regions of significant congestus heating on the flanks of the deep convection, which result in a pear-shaped bottom-heavy form of both the vertical velocity and heating profiles. Third, although weaker, the heating field expands in the upper troposphere to the rest of the domain because of the persistent extended stratiform anvils that propagate westward and coincide with the region of subsiding air. This local Hadley cell constitutes another challenge for climate models in terms of a mesoscale circulation mainly due to convection. That could impact synoptic- and/or planetary-scale flows.

As illustrated in Figs. 7 and 8, the nonlinear solution consists of convective bands aligned parallel to the shear direction and slowly moving eastward at roughly 4 m s^{-1} and westward-moving stratiform systems expanding in the perpendicular direction, propagating at roughly -11 m s^{-1}. In Figs. 10 and 11, we reproduce the associated vertical and zonal structure by averaging, in time, along the frames moving at 3.7 and -11.75 m s^{-1}, respectively. In accord with the associated heating structures, the first is called a deep convective mode, and the second is called a stratiform mode. While the deep convective mode, though markedly tilted, has mainly a first- and second-baroclinic-wind-component structure, the stratiform mode exhibits a bottom-heavy shallow circulation depicting a fourth-baroclinic-mode

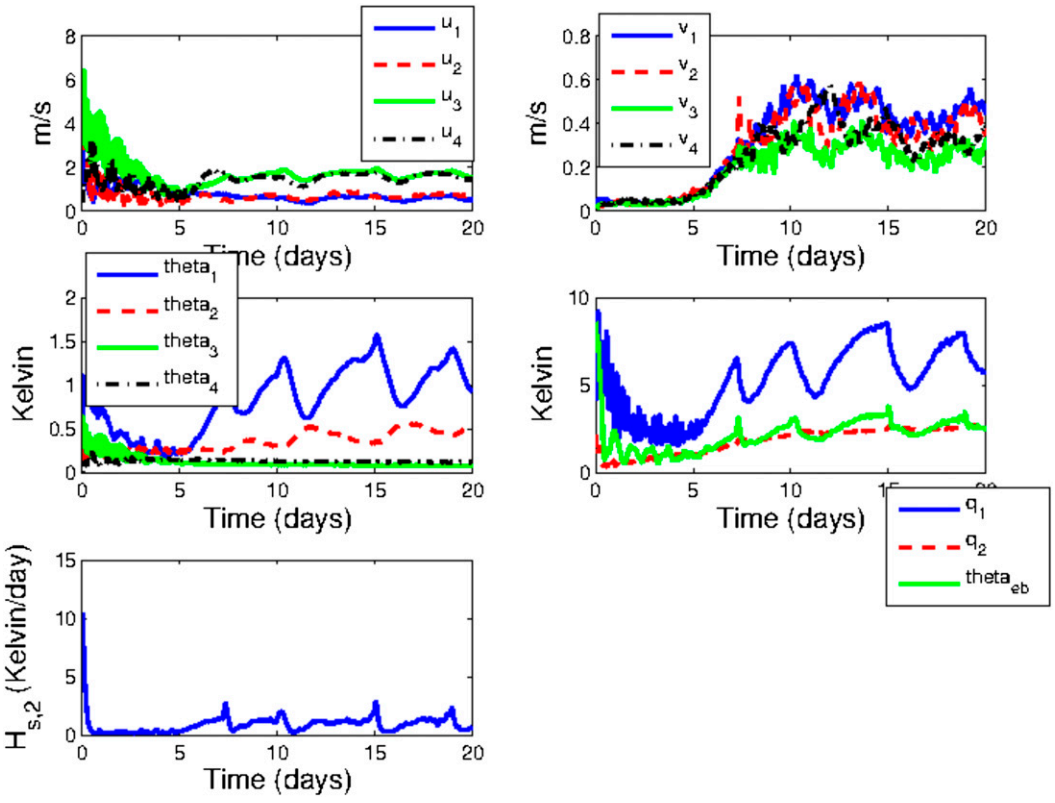

FIG. 6. Root-mean-square history of the prognostic variables during the 20 days of simulation, for the four baroclinic components of (top left) zonal velocity, (top right) meridional velocity, and (middle left) potential temperature, (middle right) the moisture variables (boundary layer θ_e, and lower- and upper-troposphere moisture), and (bottom) the adjustment stratiform heating.

structure. Clearly, the two modes strongly interact with each other through nonlinear advection, parameterized convection, downdrafts, etc., as they propagate through each other.

It is also noteworthy that both modes have significant tilts in zonal and vertical velocity components and in potential temperature, suggesting nontrivial fluxes of momentum and potential temperature. However, because of the nature of the convective mode, zonal velocity and potential temperature anomalies associated with the convective mode are relatively weak. It carries most of the deep heating anomalies, while the fluid mechanics are mostly carried by the stratiform heating mode.

In Fig. 12, we plot the time series of the vertical distribution of the domain-averaged vertical transport of the x and y momentum and potential temperature:

$$-\overline{\phi w}_z = -\frac{1}{L^2}\int_0^L\int_0^L (\phi w)_z \, dx\, dy,$$

where $L = 400$ km is the side of the square domain and $\phi = u, v, \theta$. As can be seen in all three panels of Fig. 12, the simulated solution induces significant positive and negative large-scale (wind and potential temperature) forcing (both acceleration and deceleration and heating and cooling) at various vertical levels, in all three variables. Moreover, while a period of oscillation of 8 h is visible in all three panels, there is a superimposed oscillation on a longer period of roughly 5 days, consistent with the RMS time series in Fig. 6. The 8-h time scale corresponds roughly to the period of time between two crossovers of eastward- and westward-moving waves, given that their relative speed is roughly 15.45 m s^{-1}, and the 5-day time scale may correspond to the intrinsic lifetime of the fully coupled convective–stratiform system. While the episodic interactions of the two modes is essentially an artifact of the periodic boundary conditions, in the real world there will be a multitude of successive convective bands that could interact with the same stratiform mesoalpha-scale mode during the lifetime of the latter.

Although the vertical momentum and temperature transport fluxes seem to exhibit oscillations in the vertical involving mainly the fifth-baroclinic-mode structures, a systematic projection of the different modes (results not shown) show that they also project significantly on some of the deeper modes. Moreover, there are clear episodes where the structure is mainly third baroclinic, consistent with earlier studies (Majda and Stechmann 2008; Lane and Moncrieff 2010; Khouider et al. 2012a).

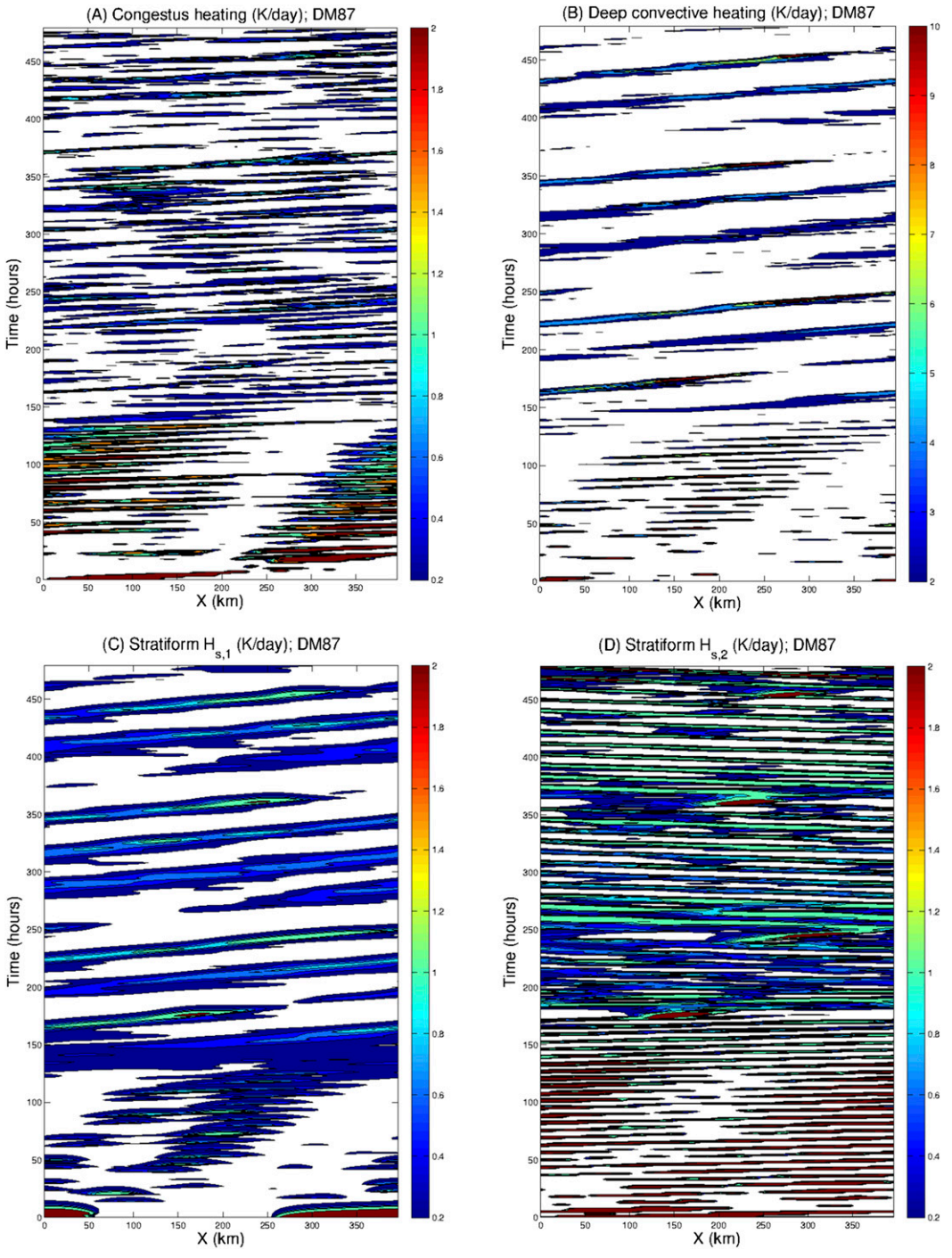

FIG. 7. Hovmöller diagrams of the (a) congestus, (b) deep, (c) lagged stratiform, and (d) large-scale condensation stratiform heating rates. All fields are averaged in the *y* direction. Note the different color scale for deep convection.

5. Discussion and conclusions

As pointed out in the introduction, shear-parallel lines of convection evolving in mesoscale stratiform systems are abundant in many regions of the globe and especially over the ITCZ of the eastern Atlantic and eastern Pacific Oceans. However, as opposed to shear-perpendicular squall lines, very little attention has been paid to the numerical simulation and dynamical modeling of these systems by the meteorological community, an exception being DM87. Yet they constitute a major challenge for climate models because they occur within the gray zone

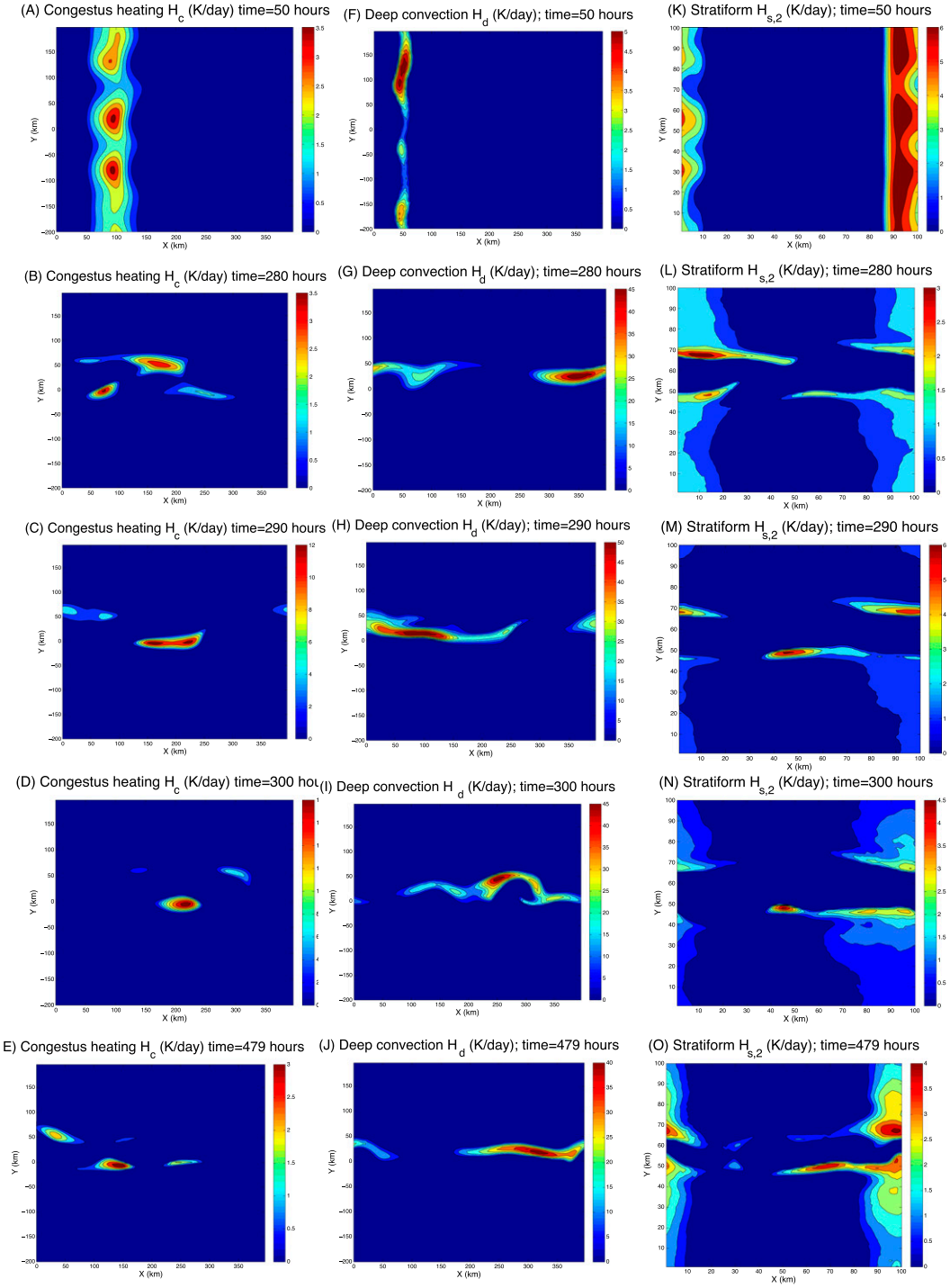

FIG. 8. Snapshots of (a)–(e) congestus, (f)–(j) deep, and (k)–(o) large-scale stratiform condensation. Snapshots are shown for (a),(f),(k) the transition period and (b)–(d),(g)–(i),(l)–(n) a 10-hourly sequence, where the cumulus events move eastward inside a narrow channel, and the extended parallel stratiform packets that move westward. A snapshot at 479 h exhibits a fully extended stratiform region.

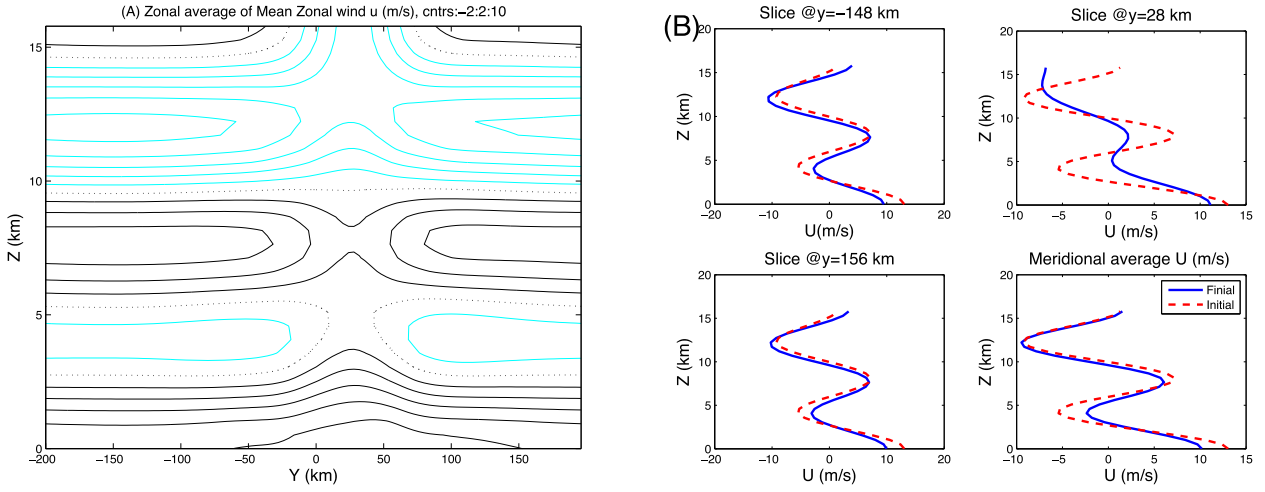

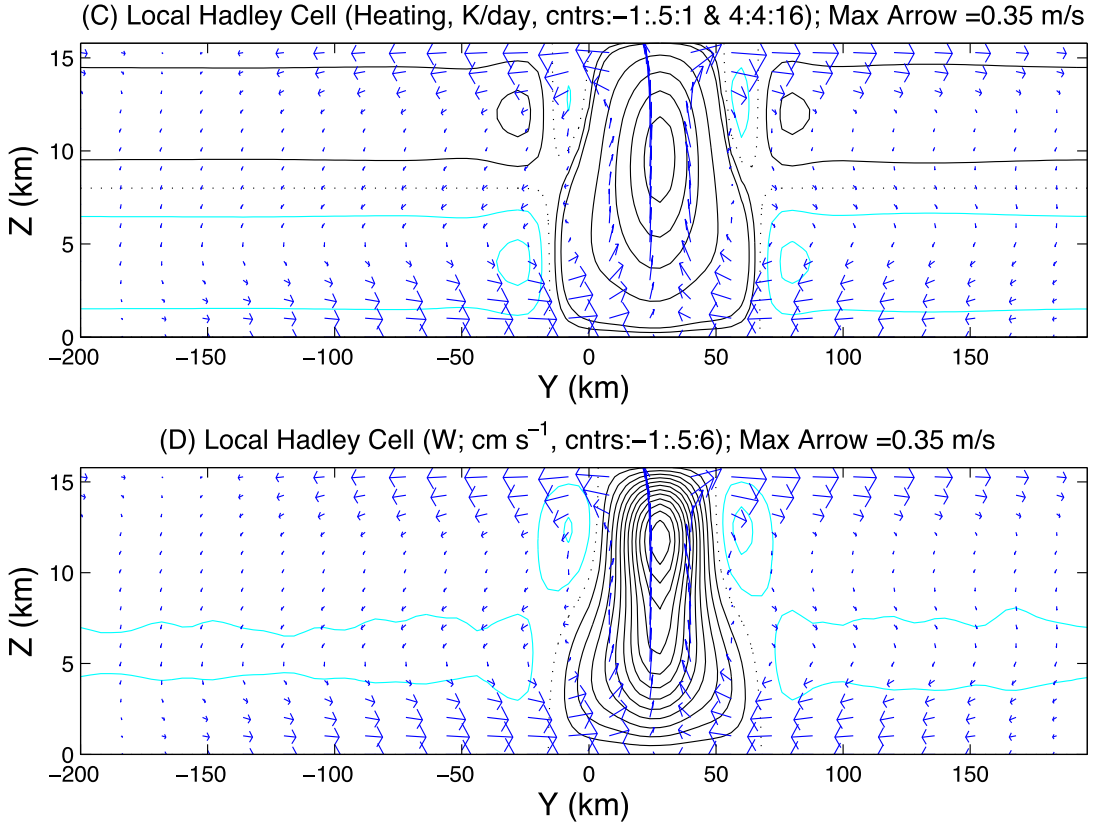

FIG. 9. Time-averaged solution for statistical equilibrium period between 7 and 20 days. (a) Zonally averaged y–z contours of zonal velocity. (b) Vertical slices of the zonally averaged mean zonal wind inside and outside the deep convection activity channel (see text) and an overall meridional mean compared to the initial background wind (dashed). (c),(d) A local Hadley-like circulation represented by the v–w velocity arrows and the total heating and vertical velocity contours. The dark lines represent positive contours, and the light colors represent negative contours. The zero contours are dashed. In (a) and (d), the contour intervals are 2 and 0.005 m s^{-1}, respectively, while in (c) it is 0.5 K day^{-1} for heating values $\leq$1 K day^{-1} and 4 K day^{-1} otherwise.

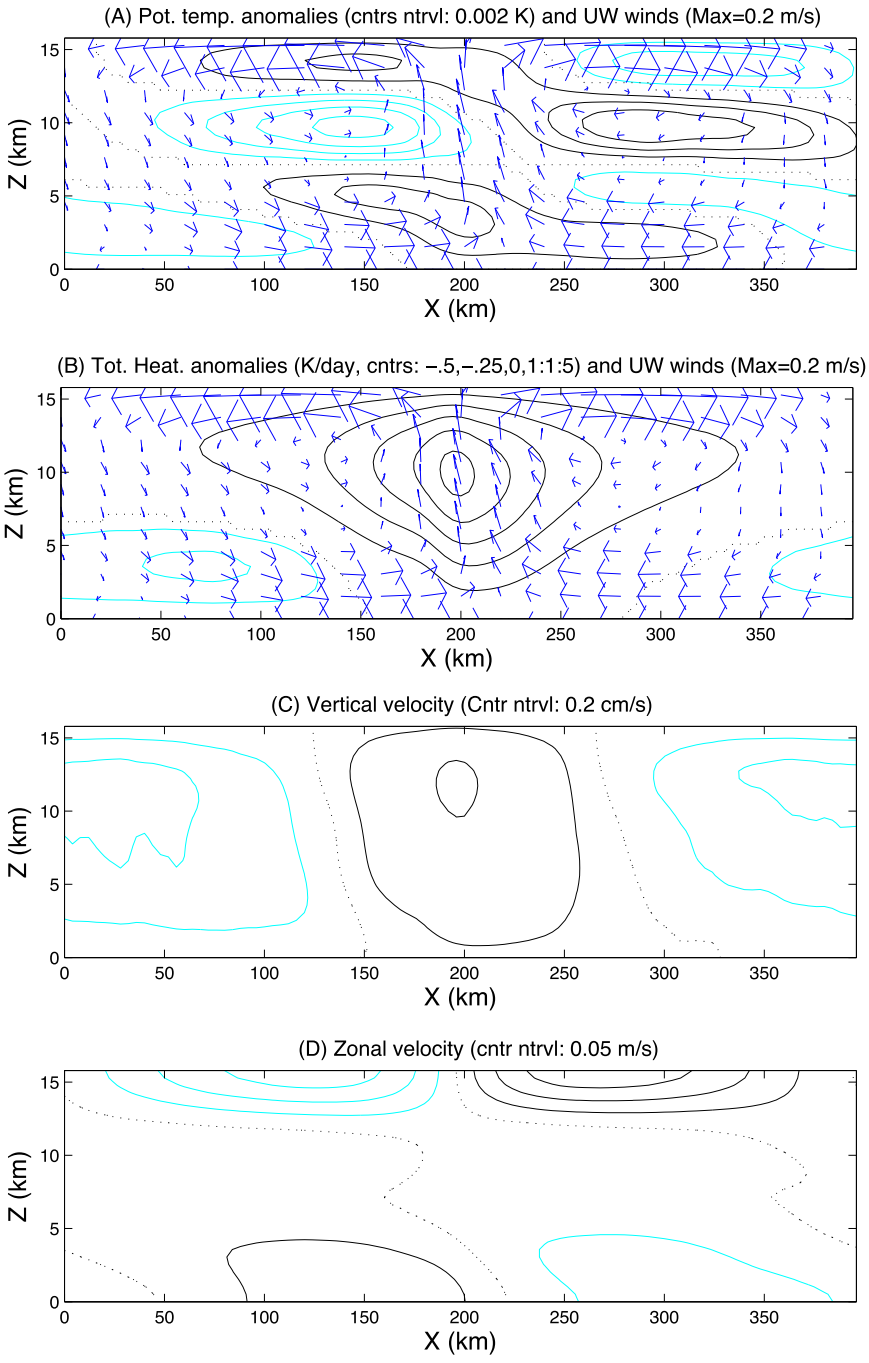

FIG. 10. Zonal and vertical structure of the eastward-moving convective mode of the nonlinear solution averaged over the last 13 days in the frame moving at 3.7 m s^{-1}. The u–w wind arrows are overlaid over the contour of (a) anomalous potential temperature and (b) total heating fields, and contours of the (c) vertical and (d) anomalous zonal velocities. Positive contours are black, negative contours are in light color, and the zero contour is dashed. The contour intervals are (a) 0.002 K, (c) 0.2 cm s^{-1}, and (d) 0.05 m s^{-1}, while in (b) they are 0.25 and 1 K day^{-1} for negative and positive values, respectively.

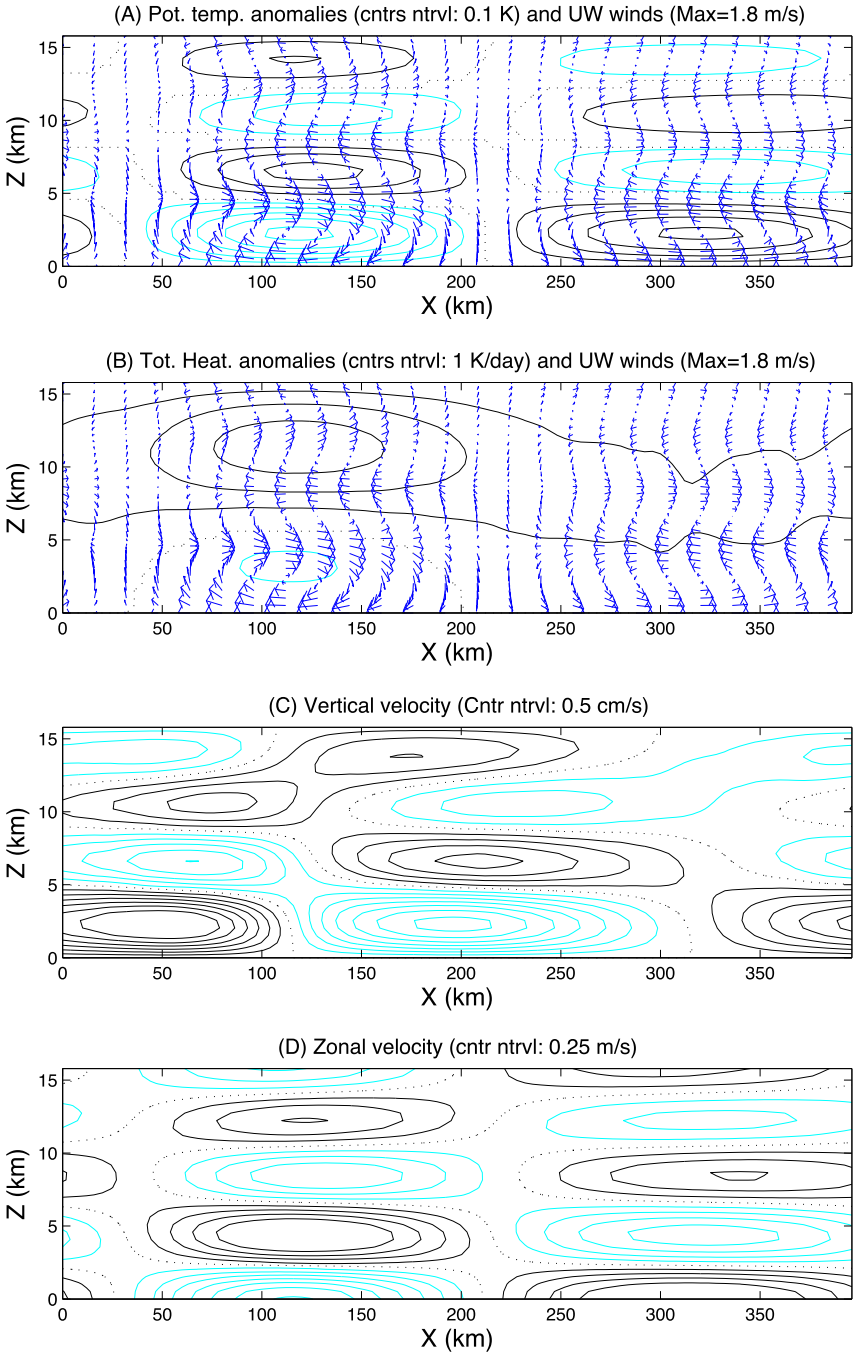

FIG. 11. As in Fig. 10, but for the westward-moving stratiform mode and the average in the frame moving at $-11.75\,\mathrm{m\,s^{-1}}$. The contour intervals are (a) 0.1 K, (b) $1\,\mathrm{K\,day^{-1}}$, (c) $0.5\,\mathrm{cm\,s^{-1}}$, and (d) $0.25\,\mathrm{m\,s^{-1}}$.

with respect to typical GCM grid resolution: too large in scale to be treated as unresolved turbulent eddies and too small to be fully resolved. There is considerable observational evidence that the associated mesoscale circulation has a nonnegligible effect on the background flow via momentum transport (LeMone 1983; LeMone et al. 1998; Tung and Yanai 2002a,b; etc.). The search for adequate parameterization schemes that take into account both the acceleration and deceleration of the synoptic- and planetary-scale flows due to upscale transfer of momentum from convective mesoscale systems has been the focus of many researchers (Moncrieff 1981, 1992; LeMone and

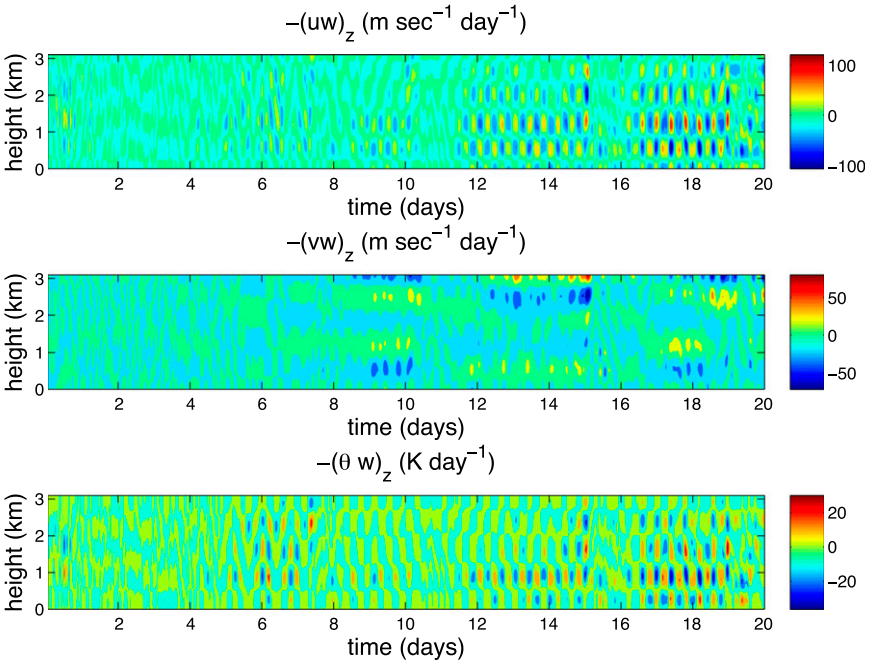

FIG. 12. Time series of domain-averaged vertical transport of (a) x momentum, (b) y momentum, and (c) potential temperature for the nonlinear simulation.

Moncrieff 1994; Wu and Moncrieff 1996; Wu et al. 2007; Song et al. 2008a,b; Majda and Stechmann 2008; Lane and Moncrieff 2010; Khouider et al. 2012a).

In this paper, we presented a simple multicloud model for shear-parallel convective systems. The original multicloud model of Khouider and Majda (KM06; KM08), which proved to be successful in representing synoptic-scale convectively coupled waves and the MJO (Khouider and Majda 2008a; Khouider et al. 2011; KM08; etc.), is extended here to mesoscale convective systems through the introduction of large-scale stratiform condensation without changing the key model parameters that are responsible for the synoptic-scale-selective instability. This approach differs from the judicious exploitation of the self-similarity property of organized convective systems to move the instability in the spectral space toward meso- and/or planetary scales (Stechmann and Majda 2009; Majda et al. 2007). Besides being able to capture simultaneously both synoptic-scale convectively coupled waves and mesoscale convective system instabilities, this new model is designed to represent the variety of mesoscale systems in terms of the alignment of their stratiform anvil region, depending on the wind shear strength and morphology of the convective organization (Parker and Johnson 2004), comprising front-leading stratiform, trailing stratiform, and parallel stratiform systems.

We first considered linear analysis for two-dimensional flows parallel to the shear direction. As reported in section 3, in the presence of the DM87 background shear, the new multicloud model exhibits three main linear instabilities corresponding to synoptic-scale waves, mesoalpha-scale systems that are directly associated with the shear effect and correspond to the stratiform anvils of the parallel systems studied in DM87, and mesobeta waves that correspond to convective-scale storms that propagate within the mesoalpha wave as sketched in Fig. 2. While both the mesoscale waves move eastward—in the direction of the low-level wind—the mesoscale beta waves have a much faster speed, 17 versus $10\,\mathrm{m\,s^{-1}}$ (see Fig. 5). We note also that in the DM87 framework there is an easterly barotropic wind component of about roughly $-10\,\mathrm{m\,s^{-1}}$. In that frame of reference, the mesoalpha waves represent the nearly standing stratiform outflows through which the convective-scale storms propagate parallel to the background shear, as depicted in DM87.

The two-dimensional linear mesoalpha-scale wave, expanded symmetrically in the y direction, was used as the initial condition for the nonlinear simulation in section 4. A small, 400 km × 400 km domain is used to focus on the mesoscale instabilities. As can be seen from Fig. 7, during the first 7 days or so, the nonlinear solution appeared as a slowly moving envelope of streaks of convection that move in the same direction at faster speeds. Consistent with the linear results in Fig. 5, the convection bands are aligned perpendicular to the background shear during the first 7 days, and the solution remained approximately two-dimensional during

this time. In other words, the main structure of the supplied initial condition was retained. Nonetheless, it is worthwhile noting the front-to-rear-tilted profile in the sense that low-level congestus heating leads deep convection, which, in turn, leads the stratiform anvils. Thus, despite the similarity of the linear solution with the DM87 shear-parallel systems, during the 7 first days, the nonlinear simulation exhibits a shear-perpendicular line of convection with lagged stratiform anvils (Parker and Johnson 2004) arising from the configuration of the initial condition.

After these 7 days, the simulated nonlinear solution enters a new statistical steady-state regime displaying fully 3D dynamics. As demonstrated in Figs. 7 and 8 and the animations (see supplemental material), the new solution consists of convective bands aligned parallel to the shear that move eastward, in the direction of the low-level wind, and essentially evolving inside a (somewhat virtual) channel. Also, large-scale stratiform anvils develop outside and perpendicular to the channel and move in the opposite direction with the upper-level winds. While deep convection occupies the center of the channel, congestus and large-scale stratiform condensation form on the flanks at both sides of the channel, although only the stratiform anvils expand in the perpendicular direction. The presence of congestus heating on the flanks is consistent with the dual structure of precipitable water in synoptic-scale westward-moving disturbance observed in satellite data by Chen et al. (2014).

The dynamical explanation of this configuration is provided by the mean solution reported in Fig. 9. Interestingly, within the channel, the mean zonal flow was altered drastically to provide a favorable environment for the parallel convective lines, while on the outside the mean zonal flow remained qualitatively the same as initially provided apart from a significant reduction in the lower jet. Also an established local Hadley-like circulation runs perpendicular to this background shear with nonnegligible meridional wind fluctuations. While the effect of this meridional circulation and the altered zonal wind, within and outside the channel, on the synoptic and/or planetary circulation remains to be investigated, these two constitute a concrete (academic) example of mesoscale flow variability directly induced by convection (i.e., through convective momentum transport) (Majda and Stechmann 2008; Lane and Moncrieff 2010; Khouider et al. 2012a). According to the Hovmöller diagrams in Fig. 7, the zonal and vertical structures associated with the eastward- and westward-moving disturbances suggest two dissociated deep convective and stratiform modes that propagate in both directions and mutually interact. They both exhibit pronounced vertical tilts that are likely responsible for the significant domain-averaged convective momentum and potential temperature vertical transport exhibited in Fig. 12.

Moreover, the profiles of heating and vertical velocity in Figs. 9c and 9d, respectively, show expected similarities and important differences as well. For example the regions of deep (in the center) and low-level congestus (on the flanks) heating are both associated with rising motion overall, although their maxima are not exactly collocated. While the maximum deep convection is somewhat in the midtroposphere, the maximum vertical velocity is located above this level, suggesting nontrivial effects of inertial forces. This is in agreement with the results of Majda et al. (2015), which suggest some limitations of the weak temperature gradient theory (Sobel et al. 2001; Majda 2007) in terms of capturing the multicloud model wave dynamics essentially from the second baroclinic mode. The stratiform mode is the larger-scale mode that occupies the whole 400 km $\times$ 400 km domain. It acts as an envelope for the deep convective events that propagate in the opposite direction. While two-way interactions between the two modes are obvious, the larger-scale stratiform mode has stronger fluid mechanics (stronger wind and temperature disturbances), and, as such, it controls the dynamics of the whole system and helps converge midtroposphere moisture toward the deep convection channel.

It is worthwhile noting that the nonlinear solution in Figs. 6–12 is not sensitive to parameters such as grid resolution, domain size, and initial condition. Although the results are not shown here for the obvious reason of space limitation and streamlining, we repeated this simulation three times, changing one parameter at a time: coarser resolution of $\Delta x = \Delta y = 8$ km; doubled y extent of the domain (i.e., 800 km); and a small initial perturbation. Except for changes in the transient time period in the third case, we obtained essentially the same dynamical structure characterized by deep convective streaks moving parallel to the shear within a virtual channel, etc. We also extended the simulation in time to 40 days, and the same statistical behavior remained. This dynamical robustness demonstrated the usefulness of the extended MCM as a parameterization for convective momentum transport in GCMs. Note that the original MCM has been used with great success as a convective parameterization (Khouider et al. 2011; Ajayamohan et al. 2013, 2014; Deng et al. 2015); it was used to represent only the convective temperature and moisture sources and sinks.

The next step is to couple the new multicloud model to a GCM. A fundamental conclusion of this paper concerns the spontaneous occurrence of mesoscale and synoptic-scale organized structures in the linear mathematical

analysis and the nonlinear simulation. This provides a dynamical explanation for the scales of organized motion evident in the satellite images depicted in Figs. 1a and 1b and an excellent example of coherent convective structures approximated by slantwise layer overturning (Moncrieff 2010). Representing such structures in a field of cumulus heralds a new era for the parameterization of organized convection in global models.

It will be interesting to perform a large-scale cloud-resolving model simulation to elucidate the role of upper-level jet and stratiform heating on the shear-parallel MCS dynamics. Moreover, some understanding of the physical mechanisms at work and the contribution of the various model components and parameters to the successful simulation of shear-parallel mesoscale convective systems can be gained using a few sensitivity tests for the 3D nonlinear model using the linear theory results in Table 4 as guidelines. Such initiatives will be considered and reported elsewhere by the authors in the near future.

Acknowledgments. This research was accomplished in large part during two successive short visits of B. K. to the National Center for Atmospheric Research, in Boulder, Colorado.

REFERENCES

Ajayamohan, R. S., B. Khouider, and A. J. Majda, 2013: Realistic initiation and dynamics of the Madden–Julian oscillation in a coarse resolution aquaplanet GCM. *Geophys. Res. Lett.,* **40,** 6252–6257, doi:10.1002/2013GL058187.

——, ——, and ——, 2014: Simulation of monsoon intraseasonal oscillations in a coarse-resolution aquaplanet GCM. *Geophys. Res. Lett.,* **41,** 5662–5669, doi:10.1002/2014GL060662.

Chen, G., Y. N. Takayabu, and C. Yokoyama, 2014: Synoptic-scale dual structure of precipitable water along the eastern Pacific ITCZ. *J. Climate,* **27,** 6288–6304, doi:10.1175/JCLI-D-14-00060.1.

Cheng, C.-P., and R. A. Houze Jr., 1979: The distribution of convective and mesoscale precipitation in GATE radar echo patterns. *Mon. Wea. Rev.,* **107,** 1370–1381, doi:10.1175/1520-0493(1979)107<1370:TDOCAM>2.0.CO;2.

Deng, Q., B. Khouider, and A. J. Majda, 2015: The MJO in a coarse-resolution GCM with a stochastic multicloud parameterization. *J. Atmos. Sci.,* **72,** 55–74, doi:10.1175/JAS-D-14-0120.1.

Dudhia, J., and M. W. Moncrieff, 1987: A numerical simulation of quasi-stationary tropical convective bands. *Quart. J. Roy. Meteor. Soc.,* **113,** 929–967, doi:10.1002/qj.49711347711.

——, ——, and D. W. K. So, 1987: The two-dimensional dynamics of West African squall lines. *Quart. J. Roy. Meteor. Soc.,* **113,** 121–146, doi:10.1002/qj.49711347508.

Dunion, J. P., and C. S. Marron, 2008: A reexamination of the Jordan mean tropical sounding based on awareness of the Saharan air layer: Results from 2002. *J. Climate,* **21,** 5242–5253, doi:10.1175/2008JCLI1868.1.

Han, Y., and B. Khouider, 2010: Convectively coupled waves in a sheared environment. *J. Atmos. Sci.,* **67,** 2913–2942, doi:10.1175/2010JAS3335.1.

Houze, R. A., Jr., 2004: Mesoscale convective systems. *Rev. Geophys.,* **42,** RG4003, doi:10.1029/2004RG000150.

——, and C. P. Cheng, 1977: Radar characteristics of tropical convection observed during GATE: Mean properties and trends over the summer season. *Mon. Wea. Rev.,* **105,** 964–980, doi:10.1175/1520-0493(1977)105<0964:RCOTCO>2.0.CO;2.

Johnson, R. H., T. M. Rickenbach, S. A. Rutledge, P. E. Ciesielski, and W. H. Schubert, 1999: Trimodal characteristics of tropical convection. *J. Climate,* **12,** 2397–2418, doi:10.1175/1520-0442(1999)012<2397:TCOTC>2.0.CO;2.

Kacimi, A., and B. Khouider, 2013: A numerical investigation of the barotropic instability on the equatorial β-plane. *Theor. Comput. Fluid Dyn.,* **27,** 491–512, doi:10.1007/s00162-012-0260-3.

Khouider, B., and A. J. Majda, 2006: A simple multicloud parameterization for convectively coupled tropical waves. Part I: Linear analysis. *J. Atmos. Sci.,* **63,** 1308–1323, doi:10.1175/JAS3677.1.

——, and ——, 2007: A simple multicloud parameterization for convectively coupled tropical waves. Part II: Nonlinear simulations. *J. Atmos. Sci.,* **64,** 381–400, doi:10.1175/JAS3833.1.

——, and ——, 2008a: Equatorial convectively coupled waves in a simple multicloud model. *J. Atmos. Sci.,* **65,** 3376–3397, doi:10.1175/2008JAS2752.1.

——, and ——, 2008b: Multicloud models for organized tropical convection: Enhanced congestus heating. *J. Atmos. Sci.,* **65,** 895–914, doi:10.1175/2007JAS2408.1.

——, A. St-Cyr, A. J. Majda, and J. Tribbia, 2011: The MJO and convectively coupled waves in a coarse-resolution GCM with a simple multicloud parameterization. *J. Atmos. Sci.,* **68,** 240–264, doi:10.1175/2010JAS3443.1.

——, Y. Han, and J. A. Biello, 2012a: Convective momentum transport in a simple multicloud model for organized convection. *J. Atmos. Sci.,* **69,** 281–302, doi:10.1175/JAS-D-11-042.1.

——, ——, A. Majda, and S. Stechmann, 2012b: Multiscale waves in an MJO background and CMT feedback. *J. Atmos. Sci.,* **69,** 915–933, doi:10.1175/JAS-D-11-0152.1.

——, A. J. Majda, and S. N. Stechmann, 2013: Climate science in the tropics: Waves, vortices and PDEs. *Nonlinearity,* **26,** R1, doi:10.1088/0951-7715/26/1/R1.

Kiladis, G. N., M. C. Wheeler, P. T. Haertel, K. H. Straub, and P. E. Roundy, 2009: Convectively coupled equatorial waves. *Rev. Geophys.,* **47,** RG2003, doi:10.1029/2008RG000266.

Kuo, H. L., 1963: Perturbations of plane Couette flow in stratified fluid and origin of cloud streets. *Phys. Fluids,* **6,** 195–211, doi:10.1063/1.1706719.

Lafore, J.-P., and M. W. Moncrieff, 1989: A numerical investigation of the organization and interaction of the convective and stratiform regions of tropical squall lines. *J. Atmos. Sci.,* **46,** 521–544.

Lane, T. P., and M. W. Moncrieff, 2010: Characterization of momentum transport associated with organized moist convection and gravity waves. *J. Atmos. Sci.,* **67,** 3208–3225, doi:10.1175/2010JAS3418.1.

LeMone, M. A., 1983: Momentum transport by a line of cumulonimbus. *J. Atmos. Sci.,* **40,** 1815–1834, doi:10.1175/1520-0469(1983)040<1815:MTBALO>2.0.CO;2.

——, and M. W. Moncrieff, 1994: Momentum and mass transport by convective bands: Comparisons of highly idealized dynamical models to observations. *J. Atmos. Sci.,* **51,** 281–305, doi:10.1175/1520-0469(1994)051<0281:MAMTBC>2.0.CO;2.

——, E. J. Zipser, and S. B. Trier, 1998: The role of environmental shear and thermodynamic conditions in determining the structure and evolution of mesoscale convective systems during TOGA COARE. *J. Atmos. Sci.,* **55,** 3493–3518, doi:10.1175/1520-0469(1998)055<3493:TROESA>2.0.CO;2.

Majda, A. J., 2003: *Introduction to PDEs and Waves for the Atmosphere and Ocean*. Courant Lecture Notes in Mathematics, Vol. 9, American Mathematical Society, 234 pp.

——, 2007: New multiscale models and self-similarity in tropical convection. *J. Atmos. Sci.,* **64,** 1393–1404, doi:10.1175/JAS3880.1.

——, and S. N. Stechmann, 2008: Stochastic models for convective momentum transport. *Proc. Natl. Acad. Sci. USA,* **105,** 17 614–17 619, doi:10.1073/pnas.0806838105.

——, ——, and B. Khouider, 2007: Madden–Julian oscillation analog and intraseasonal variability in a multicloud model above the equator. *Proc. Natl. Acad. Sci. USA,* **104,** 9919–9924, doi:10.1073/pnas.0703572104.

——, B. Khouider, and Y. Frenkel, 2015: Effects of rotation and mid-troposphere moisture on organized convection and convectively coupled gravity waves. *Climate Dyn.,* **44,** 937–960, doi:10.1007/s00382-014-2222-5.

Mapes, B. E., 2000: Convective inhibition, subgrid-scale triggering energy, and stratiform instability in a toy tropical wave model. *J. Atmos. Sci.,* **57,** 1515–1535, doi:10.1175/1520-0469(2000)057<1515:CISSTE>2.0.CO;2.

——, S. Tulich, J. Lin, and P. Zuidema, 2006: The mesoscale convection life cycle: Building block or prototype for large-scale tropical waves? *Dyn. Atmos. Oceans,* **42,** 3–29, doi:10.1016/j.dynatmoce.2006.03.003.

Moncrieff, M. W., 1981: A theory of organized steady convection and its transport properties. *Quart. J. Roy. Meteor. Soc.,* **107,** 29–50, doi:10.1002/qj.49710745103.

——, 1992: Organized convective systems: Archetypical dynamical models, mass and momentum flux theory, and parameterization. *Quart. J. Roy. Meteor. Soc.,* **118,** 819–850, doi:10.1002/qj.49711850703.

——, 2010: The multiscale organization of moist convection and the intersection of weather and climate. *Climate Dynamics: Why Does Climate Vary? Geophys. Monogr.,* Vol. 189, Amer. Geophys. Union, 3–26, doi:10.1029/2008GM000838.

——, M. Shapiro, J. Slingo, and F. Molteni, 2007: Collaborative research at the intersection of weather and climate. *WMO Bull.*, **56**, 206–211.

——, D. E. Waliser, M. J. Miller, M. A. Shapiro, G. R. Asrar, and J. Caughey, 2012: Multiscale convective organization and the YOTC virtual global field campaign. *Bull. Amer. Meteor. Soc.,* **93,** 1171–1187, doi:10.1175/BAMS-D-11-00233.1.

Parker, M. D., and R. H. Johnson, 2004: Structures and dynamics of quasi-2D mesoscale convective systems. *J. Atmos. Sci.,* **61,** 545–567, doi:10.1175/1520-0469(2004)061<0545:SADOQM>2.0.CO;2.

Rotunno, R., J. B. Klemp, and M. L. Weisman, 1988: A theory for strong long-lived squall lines. *J. Atmos. Sci.,* **45,** 463–485, doi:10.1175/1520-0469(1988)045<0463:ATFSLL>2.0.CO;2.

Sobel, A. H., J. Nilsson, and L. M. Polvani, 2001: The weak temperature gradient approximation and balanced tropical moisture waves. *J. Atmos. Sci.,* **58,** 3650–3665, doi:10.1175/1520-0469(2001)058<3650:TWTGAA>2.0.CO;2.

Song, X., X. Wu, G. J. Zhang, and R. W. Arritt, 2008a: Dynamical effects of convective momentum transports on global climate simulations. *J. Climate,* **21,** 180–194, doi:10.1175/2007JCLI1848.1.

——, ——, ——, and ——, 2008b: Understanding the effects of convective momentum transport on climate simulations: The role of convective heating. *J. Climate,* **21,** 5034–5047, doi:10.1175/2008JCLI2187.1.

Stechmann, S. N., and A. J. Majda, 2009: Gravity waves in shear and implications for organized convection. *J. Atmos. Sci.,* **66,** 2579–2599, doi:10.1175/2009JAS2976.1.

Straub, K. H., and G. N. Kiladis, 2002: Observations of a convectively coupled Kelvin wave in the eastern Pacific ITCZ. *J. Atmos. Sci.,* **59,** 30–53, doi:10.1175/1520-0469(2002)059<0030:OOACCK>2.0.CO;2.

Takayabu, Y. N., 1994: Large-scale cloud disturbances associated with equatorial waves. Part I: Spectral features of the cloud disturbances. *J. Meteor. Soc. Japan,* **72,** 433–448.

Thorpe, A. J., M. J. Miller, and M. W. Moncrieff, 1982: Two-dimensional convection in non-constant shear: A model of mid-latitude squall lines. *Quart. J. Roy. Meteor. Soc.,* **108,** 739–762, doi:10.1002/qj.49710845802.

Tung, W. W., and M. Yanai, 2002a: Convective momentum transport observed during the TOGA COARE IOP. Part I: General features. *J. Atmos. Sci.,* **59,** 1857–1871, doi:10.1175/1520-0469(2002)059<1857:CMTODT>2.0.CO;2.

——, and ——, 2002b: Convective momentum transport observed during the TOGA COARE IOP. Part II: Case studies. *J. Atmos. Sci.,* **59,** 2535–2549, doi:10.1175/1520-0469(2002)059<2535:CMTODT>2.0.CO;2.

Waliser, D. E., and Coauthors, 2012: The ''Year'' of Tropical Convection (May 2008–April 2010): Climate variability and weather highlights. *Bull. Amer. Meteor. Soc.,* **93,** 1189–1218, doi:10.1175/2011BAMS3095.1.

Wheeler, M., and G. N. Kiladis, 1999: Convectively coupled equatorial waves: Analysis of clouds and temperature in the wavenumber–frequency domain. *J. Atmos. Sci.,* **56,** 374–399, doi:10.1175/1520-0469(1999)056<0374:CCEWAO>2.0.CO;2.

Wu, X., and M. W. Moncrieff, 1996: Collective effects of organized convection and their approximation in general circulation models. *J. Atmos. Sci.,* **53,** 1477–1495, doi:10.1175/1520-0469(1996)053<1477:CEOOCA>2.0.CO;2.

——, L. Deng, X. Song, and G. J. Zhang, 2007: Coupling of convective momentum transport with convective heating in global climate simulations. *J. Atmos. Sci.,* **64,** 1334–1349, doi:10.1175/JAS3894.1.

Yanai, M., S. Esbensen, and J.-H. Chu, 1973: Determination of bulk properties of tropical cloud clusters from large-scale heat and moisture budgets. *J. Atmos. Sci.,* **30,** 611–627, doi:10.1175/1520-0469(1973)030<0611:DOBPOT>2.0.CO;2.